Strain-path change induced transients in flow stress, work hardening and *r*-values in aluminum

Tomáš Mánik [a], Bjørn Holmedal [a] and Odd Sture Hopperstad [b,c]

[a]Department of Materials Science and Engineering, Norwegian University of Science and Technology
NO-7491 Trondheim, Norway

[b]Department of Structural Engineering, Norwegian University of Science and Technology
NO-7491 Trondheim, Norway

[c]Structural Impact Laboratory (SIMLab), Center for Research-based Innovation, Norwegian University of Science and Technology NO-7491 Trondheim, Norway

tomas.manik@ntnu.no, bjorn.holmedal@ntnu.no, odd.hopperstad@ntnu.no
Corresponding author: Tomáš Mánik, Tel.: +47 40305578

Abstract

Commercially pure aluminum with random texture was prestrained either by rolling or by uniaxial compression, and then tested in uniaxial tension to study the transients in flow stress, work hardening and *r*-value induced by the strain-path change. New experimental results are reported on the variation of the *r*-value and the permanently reduced work hardening subsequent to the strain-path change. A continuum plasticity model was developed that can reproduce the observed behavior. The model applies a second-order "delayed pointer" tensor to represent the microstructural anisotropy and was implemented into the finite element software LS-DYNA. The model was calibrated to the experimental data, and a simulation of early strain localization subsequent to an orthogonal strain-path change was compared to strain fields measured by a digital image correlation technique.

1. Introduction

1.1. Microstructure and mechanical behavior after strain-path changes

The overall plastic anisotropy in metals induced by the imposed deformation may originate from different sources and at various length scales. These scales are traditionally referred to as (Peeters et al., 2001): a micro-scale defined by slip system activity, a meso-scale defined by development of a dislocation substructure composed of regions with low and high dislocation density, and a macro-scale of plastic anisotropy due to a crystallographic texture development.

In metal forming operations, material points are often subjected to multi-path loading resulting in complex strain paths. For example during deep drawing operations, following the material point that flows from the flange area to the die cavity, the strain mode changes from pure shear to biaxial tension (Esche et al., 2000). Another example is the ECAP process in which the orientation of the specimen changes between consecutive passes (Seipp et al., 2012; Sivaraman and Chakkingal, 2008; Yapici et al., 2007). Gradual or sudden deviation from proportional strain paths during deformation is for some materials, especially those with high stacking-fault energy, associated with extra hardening or softening and a transient stress and hardening-rate response can be observed. This is caused by the induced plastic anisotropy originating from previous strain paths.

It is still an open question whether transient responses to strain path changes are solely due to the heterogeneous dislocation substructure, like cells and dislocation walls formed during the previous strain-paths, i.e. anisotropy on the mesoscopic level, or if it is rather due to the nature of dislocations themselves and their interaction on the slip system level, i.e. anisotropy on the microscopic level. It was concluded by many authors that arrangement into cell walls is necessary for the transient to occur (Bate et al., 2007; Eardley et al., 2003; Jensen and Hansen, 1990; Li and Bate, 1991; Li et al., 2004; Wilson, 1994). On the contrary, Vincze et al. (2005) observed during low temperature experiments that low carbon steel showed pronounced Bauschinger effect together with a stress plateau even though no heterogeneous dislocation distribution was formed. It was thus concluded that structural features like cell dissolution are not responsible for, but merely correlated to, the observed transient hardening-rate stagnation. One can thus conclude that the cellular dislocation structure plays an important role at least in metals in which it is formed.

The typical representative and perhaps the most sensitive material to strain-path changes is IF steel, for which this phenomenon has been the subject of intensive experimental research since pioneered by Garofalo and Low (1955), and aluminum alloys. A review of the major works on these metals can be found in Barlat et al. (2003). Metals with low stacking-fault energy, where the effect of the changes in the strain paths is less pronounced, were studied as well (Hutchinson et al., 1976; Lamba and Sidebottom, 1978a, b; Li et al., 2006; Sakharova et al., 2008; Schmitt et al., 1991; Zandrahimi et al., 1989). Recently, the influence of the strain-path changes on de-twinning in hexagonal metals was studied in zirconium (Proust et al., 2010) and beryllium (Brown et al., 2012; Sisneros et al., 2010).

From the continuum mechanics point of view, any abrupt strain-path change can be quantified by one scalar parameter introduced by Schmitt et al. (1985), which serves as a measure of the strain-path change. This parameter is related to the scalar product of the plastic deformation rate tensors $\mathbf{D}_1^p$ and $\mathbf{D}_2^p$ before and after change, respectively, as

$$\cos\phi = \frac{\mathbf{D}_1^p : \mathbf{D}_2^p}{\left\|\mathbf{D}_1^p\right\| \cdot \left\|\mathbf{D}_2^p\right\|} \tag{1}$$

Monotonic loading is represented by the value $\cos\phi = 1$, strain reversal by $\cos\phi = -1$. The value $\cos\phi = 0$ represents an orthogonal sequence of deformation modes, because the deformation rate tensors make an angle of 90°. When the value of $\cos\phi$ is close to 1, 0 or -1, the strain-path change is called pseudo-monotonic, pseudo-orthogonal and pseudo-reverse, respectively. Note, for instance, that for strain-path changes given by the sequence of rolling and uniaxial tension in the rolling plane, one can, in theory, cover a range of Schmitt angles $\phi \in \left[0°, 120°\right]$ (see Appendix A and Fig. 13).

In the case of reverse or pseudo-reverse tests, the Bauschinger effect (Bauschinger, 1881) normally occurs. It refers to a decrease of yield strength after reloading, followed by a transition zone characterized by work-hardening stagnation. This process is sometimes called the macro Bauschinger effect (Brown and Stobbs, 1971; Hu et al., 1992). Between yielding and work-hardening stagnation, there is a range of 1-2% strain of very high work hardening (Barlat et al., 2003; Wilson et al., 1990). This is also referred to as the micro-Bauschinger effect (Hu et al., 1992).

The cross-hardening effect, which is strongest during orthogonal strain-path changes, refers to the increase of the yield strength typically followed by a softening zone and resumption of work-hardening. After a sufficiently large pre-deformation, the work-softening can lead to instability, because the subsequent increase in work hardening may be insufficient to compensate the geometrical softening, and the result is very early strain localization and necking (Li and Bate, 1991). The influence of strain-path changes on ductility and formability has been the subject of many studies (Ghosh and Backofen, 1973; Hutchinson et al., 1976; Hutchinson and Davis, 1983; Laukonis, 1979; Laukonis and Ghosh, 1978; Li and Bate, 1991; Lloyd and Sang, 1979; Wagoner and Laukonis, 1983; Wilson et al., 1990; Zandrahimi et al., 1989). To our knowledge, only few simulations have been performed with the aim to study strain localization after a strain-path change (see e.g. Hoc et al. (2001); Yoshida and Kuroda (2012); Franz et al. (2013),(Butuc et al., 2010; Butuc et al., 2011; da Rocha et al., 2009)). Korbel and Martin (1988) used a photographic technique to detect localized necking after strain-path change. The digital image correlation (DIC) technique has become increasingly popular for revealing the strain field in mechanical experiments (Benallal et al., 2008; De Codes et al., 2011; Rastogi, 2000; Roux et al., 2008; Sutton et al., 2000).

Peeters et al. (2000) assumed that strain-path changes in IF steels introduced only transient changes in the stress-strain curves, which vanish after a certain strain, from which the stress-strain curves tend to follow the behavior of the monotonic curve of the new deformation mode. However, while changes in work hardening are transient, the flow stress can be influenced permanently (Li and Bate, 1991; Sun and Wagoner, 2013; Wilson et al., 1990; Zandrahimi et al., 1989). This is referred to as permanent softening (Brown, 1977; Wilson et al., 1990). Even when this transient behavior vanishes after a certain strain and follows the behavior dictated by the new strain path, it can influence the formability in a negative manner by bringing on earlier strain localization. It is thus important that such mechanical behavior upon strain-path changes is included in constitutive models.

1.2. Models

From the modeling point of view, transients related to strain-path changes have been approached either by phenomenological continuum plasticity theory with the intention to mimic microstructural changes by introducing additional internal variables, or by using physically-based models taking advantage of the crystal plasticity framework, Peeters et al. (2000), Holmedal et al. (2008). While crystal plasticity models are computationally demanding when applied in finite element simulations on industrial scale, the additional computational cost paid in continuum plasticity models for implementing the constitutive relations required for capturing strain-path changes is low. On the other hand, when building multiscale modelling frameworks, polycrystal plasticity models enable transfer of physical parameters determined by micro-scale models, e.g. at the atomistic or molecular level (Roters et al., 2010).

In continuum plasticity models, the plastic anisotropy of a material at any instance is represented by the shape of the yield function, which in the case of a quadratic yield locus can be written in the form

$$\bar{\sigma} \equiv \sqrt{(\mathbf{\Sigma}-\mathbf{X}):\boldsymbol{\mathcal{A}}:(\mathbf{\Sigma}-\mathbf{X})} = \sigma_Y \tag{2}$$

where $\mathbf{\Sigma}$ is a stress tensor depending on the formulation applied, e.g. Cauchy, second Piola-Kirchhoff or Mandel stress, $\mathbf{X}$ is the backstress tensor, $\boldsymbol{\mathcal{A}}$ is a fourth-order tensor representing the yield locus, $\bar{\sigma}$ is the effective stress and σ_Y is the yield stress. There are two ways to incorporate the effect of strain-path changes on the flow stress and the hardening rate in the continuum plasticity framework. One group of models tries to modify the shape of the yield locus, i.e. by changing the tensor $\boldsymbol{\mathcal{A}}$ by either rotating or distorting it (Baltov and Sawczuk, 1965; Barlat et al., 2011; Barlat et al., 2013; Barthel et al., 2008; Choi et al., 2006; Feigenbaum and Dafalias, 2007; Francois, 2001; Ishikawa, 1997; Ishikawa and Sasaki, 1998; Levkovitch and Svendsen, 2007b, a; Noman et al., 2010; Pietryga et al., 2012). The yield surface distortion during both proportional and non-proportional strain paths was also observed experimentally (Khan et al., 2009; Khan et al., 2010a, b; Pandey et al., 2013). The fourth-order tensor $\boldsymbol{\mathcal{A}}$ is modified according to an evolution equation. In order to take the effect of strain-path changes into account, $\boldsymbol{\mathcal{A}}$ is usually additively split into the parts parallel and orthogonal to the current plastic flow direction. Note, however, that high-exponent anisotropic yield loci cannot be expressed in the form of Eq. (2).

Recently, a more general distortion of any type of isotropic or anisotropic yield locus was introduced by Barlat et al. (2011) as an alternative to kinematic hardening. This model was implemented numerically by Lee et al. (2012). The model was first used in applications, taking into account orthogonal hardening, by Barlat et al. (2013), employing the model of Rauch et al. (2011) to modify the yield stress σ_Y. Later this was incorporated into extra distortion of the yield locus by Ha et al. (2013). Some enhancements to the anisotropic hardening model were recently presented by Barlat et al. (2014).

The other group of models modifies the yield stress σ_Y, while keeping the shape of the yield locus, as defined by $\boldsymbol{\mathcal{A}}$, constant. This was proposed by Teodosiu and Hu (1995) and later re-formulated for robust handling of continuous strain-path changes (Wang et al., 2008; Wang et al., 2006). At yielding, the effective stress $\bar{\sigma}$ can then be written as

$$\bar{\sigma} = \sigma_0 + R + f\,\|\boldsymbol{\mathcal{S}}\| \tag{3}$$

where σ_0 is the initial yield stress, R is the isotropic hardening and the scalar $f\,\|\boldsymbol{\mathcal{S}}\|$ represents the contribution from persistent dislocation structures. Modeling of directional hardening caused by evolution and reorientation of planar dislocation structures formed during monotonic loading is carried out by evolution of the fourth-order tensor $\boldsymbol{\mathcal{S}}$, describing the anisotropic contribution of directional dislocation structures to the flow stress. In theory the arithmetic operations involving the fourth-order tensor $\boldsymbol{\mathcal{S}}$ make this rather complex model computationally expensive (more than 50 scalar equations to solve) but in practice this can be avoided and implemented quite efficiently in a simplified manner (Haddag et al., 2007).

The Teodosiu-Hu model involves several material parameters, and mechanical testing and inverse modeling are required to identify these parameters. Strategies for the parameter identification and sensitivity analysis were treated by Haddadi et al. (2006). Despite of the model's complexity, it has become very popular (Boers et al., 2010; Bouvier et al., 2005; da Rocha et al., 2009; Flores et al., 2007; Oliveira et al., 2007; Thuillier et al., 2010). A texture-based anisotropic yield surface was incorporated by Hiwatashi et al. (1997), Li et al. (2003) and Reis et al. (2002), while strain-rate and temperature sensitivity was included by Uenishi and Teodosiu (2004). The model by Rauch et al. (2011), combined with the kinematic hardening, was adopted also in this framework by Carvalho-Resende et al. (2013). A comparison of the Teodosiu-Hu model and the model proposed by Levkovitch and Svendsen (2007b) was done by

Van Den Boogaard and Van Riel (2009) and Clausmeyer et al. (2009). The thermodynamic consistency of these models has been discussed recently by Shi and Mosler (2013).

With respect to results presented in the current paper, it is important to note that the Teodosiu-Hu model predicts transients that fade out and do not affect permanently the work hardening during subsequent monotonic loading.

1.3. Aim of the article

In this study, the transients in flow stress, work hardening and *r*-value after a strain-path change are studied for an as-cast, commercially pure aluminum with random texture. The material was pre-strained either by rolling or uniaxial compression before testing in uniaxial tension. The aluminum with random texture was chosen for two major reasons: firstly, to avoid a complex calibration of texture induced anisotropy; secondly, the as-cast material allowed machining of thick uniaxial tensile samples for Bauschinger tests, while at the same time sheets could be cut carefully by spark ignition. Aluminum has a weaker cross-hardening effect than the IF steels and for sufficiently low prestrains necking subsequent to the strain-path change can be avoided, allowing measurements of the *r*-value variation and subsequent work hardening in a controlled manner.

The experiments revealed several features related to the imposed strain-path changes, i.e. Bauschinger effect with stress plateau occurring after the strain-path reversal, overshoot of the flow stress, transient variation of the *r*-value and permanent reduction of the hardening after orthogonal strain-path changes for various prestrains. To capture these phenomena, the plasticity model recently proposed and briefly described in Holmedal et al. (2010) and Manik et al. (2012) was further developed by introducing two new transient work-hardening terms. Conceptually, the new model is similar to the one by Teodosiu and Hu (1995) in the way that rapid expansion/shrinkage of the yield surface handles the effects of strain-path changes, but it uses only second-order tensors, and the interpretation of the model and its parameters is straight-forward. The paper presents the mathematical formulation of the novel continuum plasticity model, a semi-implicit algorithm for temporal integration and the parameter identification from experimental data obtained from the strain-path change tests. The model was implemented in the finite element software LS-DYNA and applied in finite element simulations of strain localization subsequent to an orthogonal strain path change. The numerical results are compared to experimentally obtained force-elongation curves and strain fields acquired by a digital image correlation technique.

The experimental study is described in Section 2, while the model formulation is presented in Section 3. The parameter identification is explained in Section 4 and the results compared with the experimental data. The finite element simulations are presented in Section 5 and validated against experimental results. Section 6 contains a discussion of the proposed constitutive model and the results obtained in the study, whereas the main conclusions are presented in Section 7.

2. Experimental study

2.1. Material

In the present work, the investigated material was commercially pure, as-cast aluminum AA1050. This is a well-known material exhibiting pronounced cross-hardening effect during orthogonal strain-path changes as well as a plateau due to the stress stagnation after reverse tests with medium prestrain. The effects provoked by the strain-path changes are less pronounced in this material than in the low carbon steel, which is, however, an advantage when trying to avoid early localization.

Plates with dimensions 110×200 mm^2 and thickness 2.950±0.006 mm were cut by electrical discharge machining from the as-cast cylindrical billet with diameter 220 mm. The plates were cut in the axial and radial directions, making sure to avoid the center and the outermost parts of the billet. They were subsequently homogenized at 600°C/4h with a ramp of 100°C/h and subsequent cooled in air.

2.2. Experimental procedures

In this work, abrupt strain-path changes were introduced by a two-step sequence consisting of: a) prestraining by rolling followed by uniaxial tension in the transverse direction; and b) prestraining by uniaxial compression followed by uniaxial tension.

Rolling was made on a two-high laboratory rolling mill. The plates were rolled down to three different thicknesses of 2.880±0.003 mm, 2.706±0.011 mm and 2.630±0.012 mm, giving three different prestrains. After the respective prestraining, 7, 12 and 12 tensile samples were cut from the middle part of the plates and tested by uniaxial tension carried out using a servo-hydraulic MTS 810 testing machine. The shortest delay between the rolling and the tensile testing was 10 min, the longest delay was 400 days. All the samples were rolled, stored and tested at room temperature. A constant crosshead speed of 2 mm/min was applied in all cases. The tensile specimens cut from the pre-rolled plates were flat and both longitudinal and transverse extensometers with gauge length of 25 and 12 mm, respectively, were used. The width and parallel length of the specimens were 12 mm and 30mm, respectively.

Since the aluminum was tested in the as-cast and homogenized condition, it was expected to have random texture and isotropic behavior. To check this assumption, some preliminary tensile tests were carried out at $\alpha =$ 0°, 45° and 90° with respect to the longitudinal direction of the billet and are plotted in Fig. 1. The *r*-values are listed in the figure caption and within the experimental precision they are close to unity. Five parallel tests were performed for the 0° direction while one test was carried out for the 45° and 90° directions. It transpires that the curves are on top of each other, thus supporting the assumption of isotropic behavior.

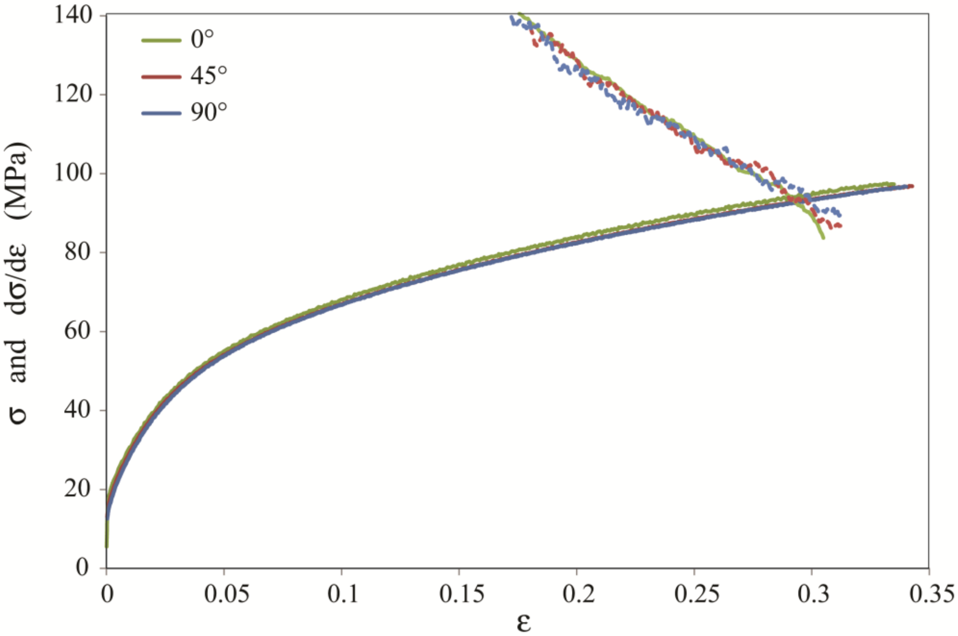

Fig. 1: True stress σ and hardening rate $d\sigma / d\varepsilon$ plotted against true strain ε from uniaxial tensile tests at 0°, 45° and 90° with respect to the longitudinal direction of the billet. The corresponding *r*-values of these tests were measured as 1.06, 1.11 and 0.95 for 0°, 45° and 90° respectively.

Referring to Hosford (2010), the yield surface calculated by the full-constraint Taylor model (Taylor, 1938) for an FCC material with initial random texture can be very well fitted by the high-exponent Hershey yield function (Hershey, 1954) with exponent $m = 8$. Adopting this criterion, the effective prestrain due to the rolling can be calculated as $\bar{\varepsilon} = 1.089 \ln\left(t_i / t_f\right)$, see Appendix A for details. For orthogonal strain-path changes, the rolling down to three different thicknesses corresponds to the effective prestrains of 5.0 ± 0.2 %, 9.3 ± 0.4 % and 12.8 ± 0.5 %, respectively. The absolute error in the effective prestrain was calculated by the error propagation due to the uncertainty in the both initial and final thickness of the plates. In the following, these prestrains will be referred to by their mean value, i.e. prestrain of 5%, 9.3% and 12.8%.

After orthogonal strain-path changes following a sufficiently large prestrain (for AA1050 aluminum greater than ~9% of effective strain), strain localization occurred at the very beginning of the second path. To study in more detail the strain localization after the orthogonal strain-path change, DIC was applied for the uniaxial tension tests on the samples with prestrain of 9.3%. The specimens were decorated with white and black paint to obtain a speckle pattern. During the tensile tests, a digital camera with resolution 1000×2050 pixels was used to acquire pictures with a frame rate of 5 Hz. The two-dimensional strain field was reconstructed by a software developed by Fagerholt (2012).

The Bauschinger tests were performed at room temperature using cylindrical specimens with diameter of 7 mm in the gauge area and an extensometer with 10 mm gauge length. These samples were made from the as-cast cylindrical billet and subjected to the same homogenization procedure as the plates used to make the flat specimens. During the Bauschinger tests, the samples were first pre-compressed to 1%, 2% or 4.4% strain, followed by tension at a constant crosshead speed of 2 mm/min in a MTS 810 servo hydraulic testing machine. For each prestrain, 2 tests were carried out. No significant buckling of the specimens was observed during the compression.

2.3. Recovery effects

Due to practical reasons, e.g. the machining the tensile specimens and the mounting in the testing machine, it is not possible to introduce uniaxial tension as a second strain path without any delay after the rolling as a first strain path. Since one has to account for some delay between the two strain paths, recovery of the dislocation substructures, built up during the first strain path, can occur. If the recovery of the strength of the pre-formed substructures causing the anisotropy is pronounced within a short time after the first strain path, one should introduce the time as an additional variable into the model.

Fig. 2a defines the overshoot $\Delta\sigma$ in a tensile test after prestraining, where the dashed curve is the monotonic stress-strain curve, while the normalized overshoot is defined as $\Delta\sigma / \sigma_{ref}$ with σ_{ref} being the flow stress at a strain equal to the prestrain in monotonic tension. The normalized overshoot $\Delta\sigma / \sigma_{ref}$ for the three different average prestrains as a function of the time delay between rolling and tensile testing is plotted in Fig. 2b. The shortest time delay was 10 min and the longest was one year. At a prestrain 12.8%, $\Delta\sigma / \sigma_{ref}$ is reduced from about 0.13 to 0.10 as the time delay is increased from 10 min to one year. The recovery seems to be even slower when smaller prestrains were applied.

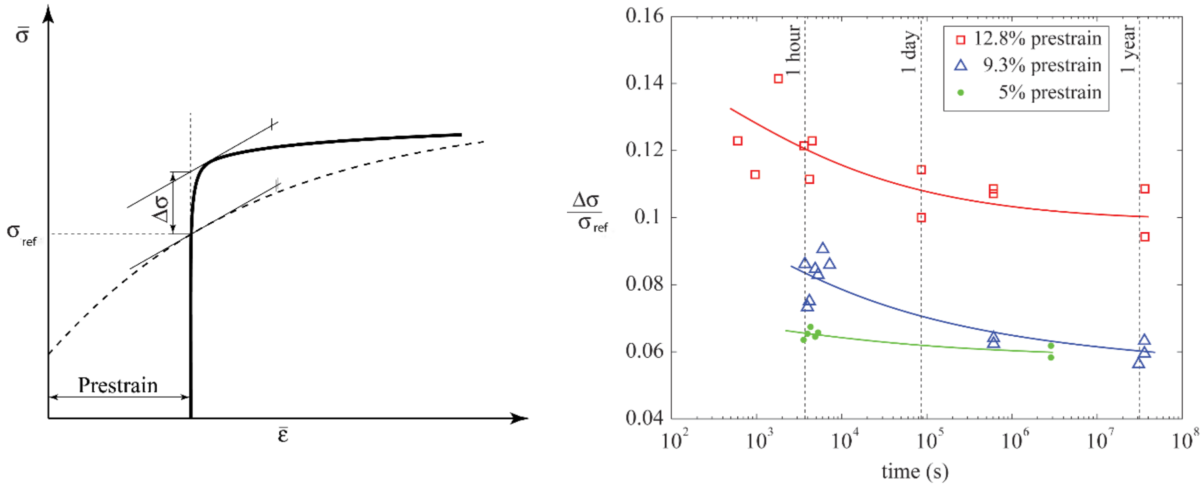

(a) (b)

Fig. 2: (a) Definition of the overshoot $\Delta\sigma$ and the reference flow stress σ_{ref} after an orthogonal strain-path change. (b) The normalized overshoot $\Delta\sigma / \sigma_{ref}$ of the flow stress due to orthogonal strain-path changes after various time delays for three different prestrains.

2.4. Experimental results

The results of orthogonal strain-path changes introduced by the sequence of rolling followed by uniaxial tension in the transverse direction for three prestrain levels are shown in Fig. 3. The effective stress-strain curves and the work-hardening rates are presented in Fig. 3a, while more details of the transient cross-hardening effect and the permanent softening are shown in Fig. 3b. Fig. 2b indicates a certain increase in the scatter of the data with increase of the prestrain. A reason for this lies in the heterogeneity of the strength and orientation of the dislocation substructures formed at larger prestrains. The experimental curves plotted in Fig. 3 were chosen as the representative ones.

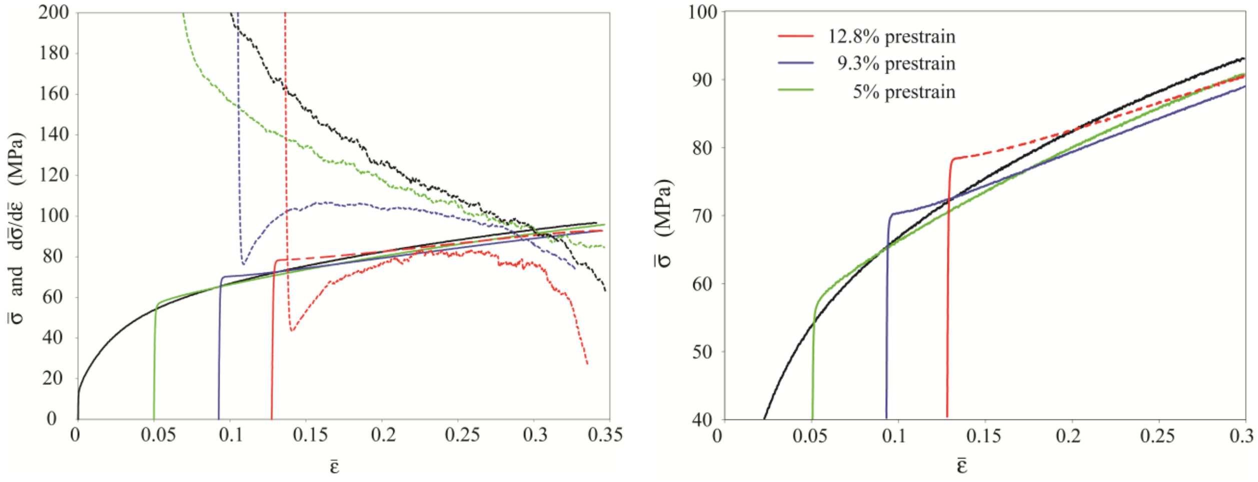

(a) (b)

Fig. 3: (a) Effective stress $\bar{\sigma}$ vs. effective plastic strain $\bar{\varepsilon}$ after orthogonal strain-path changes for prestrains of 5%, 9.35% and 12.8% plotted together with the monotonic curve. Hardening rates $d\bar{\sigma}/d\bar{\varepsilon}$ are shown by dashed curves. (b) More detailed picture of the transient cross effect and permanent softening.

A characteristic overshoot of the stress at the very beginning of the second strain path is clearly observed at all prestrains tested. It is then followed by rapid decrease in work hardening. The three prestrains tested show three different behaviors of the work hardening. While for 5% prestrain, the work hardening decreases monotonically until the onset of the diffuse necking at a strain ~30%, there is an inflexion point at about 1-2% strain after the beginning of the uniaxial tension for prestrains 9.3% and 12.8%. At a prestrain of 9.3%, the condition of uniform deformation in the whole sample remains valid during uniaxial tension until the final diffuse neck occurs. This happened, similarly as for both the monotonic curves and that with a prestrain of 5%, at a strain about 30%. However, in the case of 12.8% prestrain, the Considère criterion is reached before the inflexion point. From this point on, the true stress-true strain curve calculated based on the assumption of the uniform deformation is not correct (this part of the curve is marked long-dashed).

The strain field obtained by DIC in a tensile test with 9.3% prestrain by rolling is shown in Fig. 4 for three strain levels. The strain shown in the figure is the effective von Mises strain, here defined as $\varepsilon_{VM} = \frac{2}{\sqrt{3}}\sqrt{\varepsilon_1^2 + \varepsilon_2^2 + \varepsilon_1\varepsilon_2}$. Fig. 4A clearly illustrates that incipient diffuse necking occurs at reloading in tension, but due to the increasing work-hardening rate, the diffuse neck is not able to develop further. Thereafter the whole sample deforms rather uniformly, see Fig. 4B and Fig. 4C, until the necking again occurs at an engineering strain of ~25%. One can, however, still observe local variations in strain throughout the specimen.

For the tensile tests with an effective prestrain of 5% by rolling, the *r*-value was evaluated based upon data from two extensometers measuring both the strain ε along the tension direction and the width strain ε_w. The thickness strain ε_t was obtained based on the assumption of volume conservation as $\varepsilon_t = -\varepsilon - \varepsilon_w$. The elastic part of the strain was very small and corrections were not required for this soft material. By fitting the data for ε_w versus ε_t by a sixth-order polynomial the *r*-value was then estimated as $r = d\varepsilon_w / d\varepsilon_t$. The evolution of the *r*-value in tension after 5% prestrain by rolling is plotted in Fig. 5. Results are shown for all parallel tests. It is evident from the figure that the *r*-value exhibits a transient evolution due to the strain-path change but saturates at unity for large tensile strains.

The results from the Bauchinger tests, in which the cylindrical specimen was first compressed to prestrain of 1%, 2% or 4.4% and then loaded in tension, are presented in Fig. 6. The Bauschinger effect is clearly seen for all three prestrain levels. While the reloading curves approach the monotonic stress-strain curve for the two lower prestrains, a permanently lower flow stress is obtained for the higher prestrain of 4.4%. The initial plateau of reduced work hardening is clearly seen at the largest prestrain, but is less pronounced at the two smaller ones. The permanent softening after a strain-path change will be accounted for in the continuum plasticity model proposed in the following.

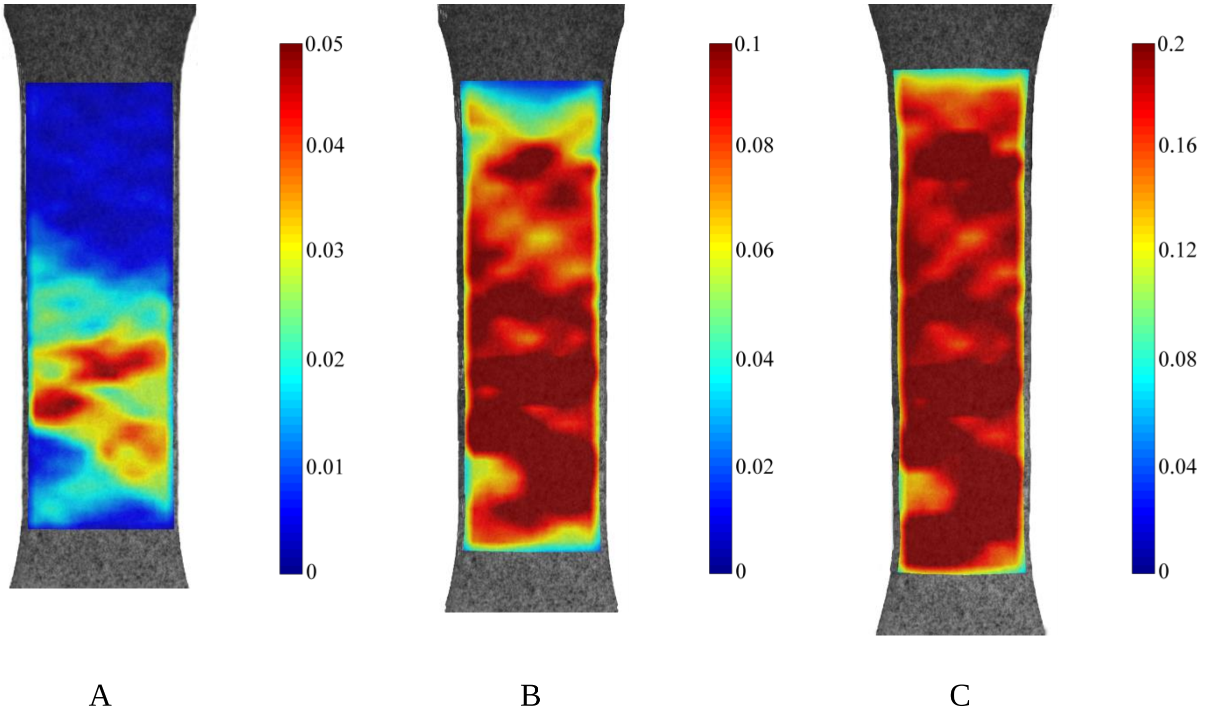

Fig. 4: Strain maps of the reduced section of the tensile specimen evaluated at engineering strain of 0.024 (A), 0.09 (B) and 0.2 (C) after prestrain to 9.3% in rolling. The effective von Mises strain is shown as a convenient measure of the 2D strain field extracted by the DIC.

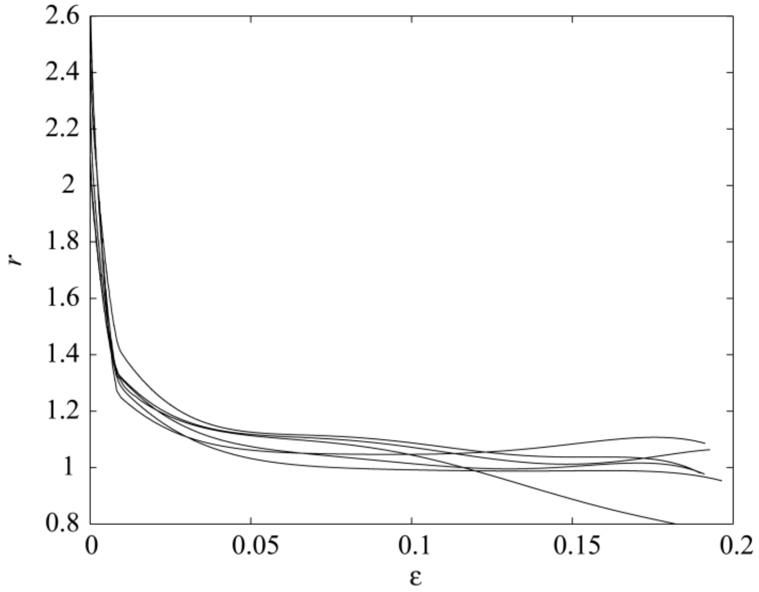

Fig. 5: Measured *r*-values plotted against the true strain *ε* during the tensile tests after orthogonal strain-path changes with a prestrain of 5% by rolling.

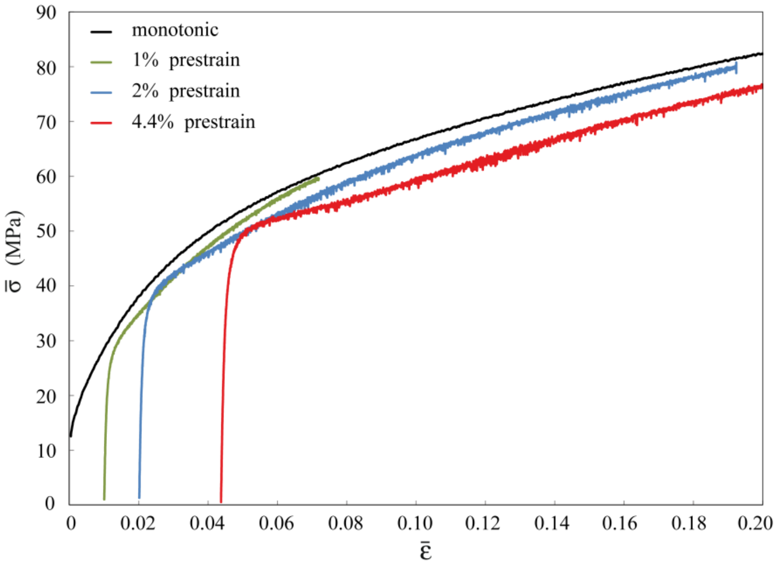

Fig. 6: Experimental results of the reverse strain-path change introduced by the sequence compression – tension, with 1%, 2% and 4.4% prestrain, together with the monotonic stress-strain curve.

3. The model formulation

The modelling framework is continuum plasticity with a yield surface and a co-rotational formulation with associated hardening, where standard isotropic and kinematic hardening rules are adopted. The sudden expansion or contraction of the yield surface subsequent to strain path changes is controlled by the "delayed pointer", i.e. a second-order tensor representing the microstructural response, with evolution as described in Section 3.4. A new model for modified hardening due to strain path changes is suggested and explained in Section 3.5. The algorithm used for the numerical implementation into FEM is outlined in Appendix B.

3.1. The yield function

In the present work, the classical rate-independent, hypo-elastic plastic formulation was employed. In this formulation, the energy is only approximately conserved in a closed elastic deformation cycle but assuming small elastic strains, the error is insignificant (Belytschko et al., 2000). In order to assure applicability of the proposed model for anisotropic materials, the corotational stress formulation is adopted to satisfy the principle of material-frame indifference. Thus, all the constitutive equations are expressed in a coordinate system that rotates with the material element. This makes the relations invariant to superposed rigid body rotations.

The corotational Cauchy stress tensor $\hat{\boldsymbol{\sigma}}$ and the corotational deformation rate tensor $\hat{\mathbf{D}}$ are defined by

$$\hat{\boldsymbol{\sigma}} = \mathbf{R}^T \boldsymbol{\sigma} \mathbf{R}, \quad \hat{\mathbf{D}} = \mathbf{R}^T \mathbf{D} \mathbf{R} \tag{4}$$

where $\boldsymbol{\sigma}$ is the Cauchy stress tensor, $\mathbf{D}$ is the deformation rate tensor, and $\mathbf{R}$ is the rotation tensor that can be obtained from the deformation gradient $\mathbf{F}$ by polar decomposition; i.e. $\mathbf{F} = \mathbf{RU}$. Here $\mathbf{U}$ is the symmetric, right stretch tensor, whereas $\mathbf{R}$ is orthogonal. The corotational deformation rate tensor $\hat{\mathbf{D}}$ can be additively decomposed into elastic and plastic deformation rate tensors as

$$\hat{\mathbf{D}} = \hat{\mathbf{D}}^e + \hat{\mathbf{D}}^p \tag{5}$$

The relation between stress rate and elastic deformation rate is written as

$$\frac{D\hat{\boldsymbol{\sigma}}}{Dt} = \hat{\mathcal{C}} : \hat{\mathbf{D}}^{e} = \hat{\mathcal{C}} : \left(\hat{\mathbf{D}} - \hat{\mathbf{D}}^{p} \right) \tag{6}$$

where $\hat{\mathcal{C}}$ is the fourth-order tensor of elastic moduli. In the corotational formulation, $\hat{\mathcal{C}}$ can be anisotropic but elastic isotropy is assumed here for the aluminum AA1050, and $\hat{\mathcal{C}}$ is defined by Young's modulus E and Poisson's ratio ν.

The proposed model follows the concept of the original Teodosiu-Hu model (Teodosiu and Hu, 1995), where the response to the strain-path changes is reflected by extra expansion/shrinkage of the yield surface, i.e. by modifying the yield stress σ_Y. The yield condition is written in the form

$$\begin{aligned} & f(\hat{\mathbf{S}}) = \varphi(\hat{\mathbf{S}}) - \sigma_Y = 0 \\ & \hat{\mathbf{S}} = \hat{\boldsymbol{\sigma}} - \hat{\mathbf{X}} \\ & \sigma_Y = R + S_o + S_r \end{aligned} \tag{7}$$

where $\hat{\mathbf{S}}$ is the corotational overstress tensor, $\hat{\mathbf{X}}$ is the corotational backstress tensor and R embodies the initial yield stress and the isotropic hardening. The scalars S_o and S_r represent the extra strength contribution due to the built-up anisotropy during the earlier straining in the orthogonal and reverse directions, respectively. The effective stress with respect to the backstress is defined by the yield function as $\bar{\sigma} \equiv \varphi(\hat{\mathbf{S}})$.

The plastic anisotropy resulting from the crystallographic texture is reflected by the yield function $\varphi(\hat{\mathbf{S}})$ which is an arbitrary admissible positive, convex and homogeneous function of degree one of $\hat{\mathbf{S}}$. In the current study, the isotropic, high-exponent Hershey yield function (Hershey, 1954) is used

$$\varphi\left(\hat{\mathbf{S}}\right) = \left(\frac{1}{2} \left(\left| \hat{S}_1 - \hat{S}_2 \right|^m + \left| \hat{S}_2 - \hat{S}_3 \right|^m + \left| \hat{S}_3 - \hat{S}_1 \right|^m \right) \right)^{1/m} \tag{8}$$

where $\hat{S}_1, \hat{S}_2, \hat{S}_3$ are the principal values of $\hat{\mathbf{S}}$. This is a reasonable choice since the as-cast and homogenized aluminum AA1050 was shown to exhibit isotropic behavior. The exponent m is not considered as a fitting parameter. It reflects the crystallographic structure of the modeled material by setting its value to 8 for FCC and 6 for BCC materials (Barlat, 1987).

The associated flow rule is adopted here giving the plastic strain rate tensor as

$$\hat{\mathbf{D}}^p = \dot{\lambda}\frac{\partial f}{\partial \hat{\mathbf{S}}} \tag{9}$$

where $\dot{\lambda}$ is the plastic multiplier governing the magnitude of the plastic flow. The plastic multiplier is then defined by the loading/unloading conditions in Kuhn-Tucker form

$$f \leq 0, \quad \dot{\lambda} \geq 0, \quad \dot{\lambda} f = 0 \tag{10}$$

3.2. Isotropic hardening

The present model is not restricted to any particular hardening rule, and two isotropic hardening terms R_i with *i*=1,2 are included allowing a very precise fit. One term will be sufficient in many applications. In the present work, the extended Voce hardening rule (Voce, 1948) is used for these two isotropic contributions to the hardening

$$\dot{R}_i = h_{R_i}\dot{\lambda}, \quad h_{R_i} = \frac{R_i^{sat} - R_i}{\Delta\varepsilon_{R_i}}, \quad i = 1,2 \tag{11}$$

where R_i^{sat} and $\Delta\varepsilon_{R_i}$ are fitting parameters, and $R_i\left(0\right) = 0$ are the initial values of the isotropic hardening terms. The parameter R_i^{sat} is the saturation value of hardening term R_i, while $\Delta\varepsilon_{R_i}$ gives the strain scale of the saturation process. Eq. (11) has analytical solutions

$$R_i = R_i^{sat}\left(1 - \exp\left(-\frac{\bar{\varepsilon}}{\Delta\varepsilon_{R_i}}\right)\right), \quad i = 1,2 \tag{12}$$

where $\bar{\varepsilon} = \int_0^t \dot{\lambda} dt$ is the effective plastic strain. In the special case of isotropic hardening, i.e., in absence of other hardening terms, the total hardening can be written as $R = R_0 + \sum_{i=1}^{2} R_i$, where R_0 is the yield stress.

3.3. Kinematic hardening

The backstress tensor is modeled by employing a nonlinear Armstrong-Frederick type of evolution rule (Armstrong and Frederick, 1966). In a similar way as for the extended Voce rule, the extended form of the Armstrong-Frederick rule was used as

$$\hat{\mathbf{X}} = \sum_{i=1}^{2} \hat{\mathbf{X}}_i, \quad \dot{\hat{\mathbf{X}}}_i = \hat{\mathbf{h}}_{X_i} \dot{\lambda}, \quad \hat{\mathbf{h}}_{X_i} = \frac{1}{\Delta\varepsilon_{X_i}} \left(X_i^{sat} \frac{\hat{\mathbf{S}}^{\text{dev}}}{\bar{\sigma}} - \hat{\mathbf{X}}_i \right) \tag{13}$$

with initial values $\hat{\mathbf{X}}_i(0) = \mathbf{0}$ of the kinematic hardening terms; X_i^{sat} and $\Delta\varepsilon_{X_i}$ are fitting parameters; $\hat{\mathbf{S}}^{\text{dev}}$ is the deviatoric part of $\hat{\mathbf{S}}$. Two terms are required because of the fast initial variation of the *r*-value as seen in Fig. 5 and the initial rapid hardening after the reverse strain-path change revealed in Fig. 6. The parameter X_i^{sat} governs the saturation value of $\hat{\mathbf{X}}_i$, while $\Delta\varepsilon_{X_i}$ defines the strain scale of the saturation process.

3.4. The “Delayed Pointer”, orthogonal and reverse hardening

In order to capture the essence of the straining history, similarly as in the Teodosiu-Hu model, the second-order, dimensionless tensor $\mathbf{P}$, denoted the “delayed pointer” tensor, is employed evolving according to an evolution equation expressed in the corotational frame as

$$\dot{\hat{\mathbf{P}}} = \hat{\mathbf{h}}_P \dot{\lambda}, \quad \hat{\mathbf{h}}_P = \frac{1}{\Delta\varepsilon_P} \left(\hat{\mathbf{N}} - \hat{\mathbf{P}} \right) \tag{14}$$

where $\hat{\mathbf{P}} = \mathbf{R}^T \mathbf{P} \mathbf{R}$ is the corotational delayed pointer tensor; $\hat{\mathbf{N}} = \hat{\mathbf{D}}^p / \|\hat{\mathbf{D}}^p\|$ is the normalized plastic strain rate tensor, and $\Delta\varepsilon_P$ is a parameter. In the original paper of Teodosiu and Hu (1995), $\hat{\mathbf{P}}$ is associated with the existence of planar directional persistent dislocation substructure formed during the previous straining. Considering the ongoing discussion initiated by Vincze et al. (2005) questioning the sole responsibility of the heterogeneous dislocation substructures for the mechanical response after strain-path changes, $\hat{\mathbf{P}}$ is given a more general meaning in this article. The magnitude and direction of $\hat{\mathbf{P}}$ relate to the strength and the alignment of the pre-built anisotropic structure, respectively, on both the slip system and mesoscopic levels. It thus does not refer exclusively to the directionality of planar dislocation walls, but rather to complex anisotropic contributions originating from both the microscopic (or slip system) and mesoscopic (or dislocation substructures) levels.

For well-annealed materials, the initial value of $\hat{\mathbf{P}}$ is justified to be zero. During the monotonic loading, $\hat{\mathbf{P}}$ is pointing in the direction $\hat{\mathbf{N}}$ of the recent (plastic) strain path and increasing in magnitude towards unity. It saturates at a strain scale given by the parameter $\Delta\varepsilon_P$. If after some prestrain, a continuous or rapid strain-path change is introduced by changing the direction of $\hat{\mathbf{N}}$, $\hat{\mathbf{P}}$ will be attracted towards $\hat{\mathbf{N}}$ as dictated by Eq. (14). To monitor the degree of strain-path change, the angle ϕ is introduced as

$$\cos\phi = \frac{\hat{\mathbf{P}} : \hat{\mathbf{N}}}{\|\hat{\mathbf{P}}\|} \tag{15}$$

It is noted that ϕ is basically the Schmitt angle characterizing the strain-path change between the current strain direction $\hat{\mathbf{N}}$ and the "delayed pointer" direction $\hat{\mathbf{P}}$.

A rapid transient isotropic expansion and shrinkage was modeled in Teodosiu and Hu (1995) by employing a fourth-order tensor representing the directionality of the dislocation structure. The present model is similar but simpler. The extra strength due to the orthogonal and pseudo-orthogonal strain-path change is modeled here by a scalar S_o as introduced in Eq. (7). The evolution of the scalar quantity S_o is given, similarly to Eq. (14), as

$$\dot{S}_o = h_{S_0}\dot{\lambda}, \quad h_{S_o} = \frac{S_o^{sat}\|\hat{\mathbf{P}}\|\sin\phi - S_o}{\Delta\varepsilon_o}, \quad S_o^{sat} = q_o R \tag{16}$$

The constant q_o relates the maximum extra strength contribution to the isotropic hardening R and $\Delta\varepsilon_o$ represents a strain scale for the transient cross hardening to take place. The initial value of S_o is zero. Subsequent to the strain-path change S_o rapidly saturates towards $S_o^{sat}\|\hat{\mathbf{P}}\|\sin\phi$, but softening will occur due to the rotation and/or change of magnitude of $\hat{\mathbf{P}}$ given by the strain scale $\Delta\varepsilon_P$ such that normally $\Delta\varepsilon_P > \Delta\varepsilon_o$. Eventually $\hat{\mathbf{P}}$ rotates into the same direction as the current $\hat{\mathbf{N}}$, and the contribution from S_o vanishes.

During reverse strain-path changes, a combination of several contributions can be responsible for the final shape of the stress-strain curve. Initially, right after the reloading, the hardening rate reaches very high values during a very small strain increment, followed by a very low hardening rate and stress stagnation taking place on a distinctly longer strain scale. Eventually, the hardening rate recovers and increases, so that the stress-strain curve tends towards the monotonic one. Sometimes, permanent softening can occur as a result of the transient changes in the hardening. Similarly as for an orthogonal strain-path change, the induced anisotropy built-up during the prestrain contributes by an additional strength S_r when reversal or pseudo-reversal of the strain-paths is made. This contribution is modeled here in a similar fashion as for the cross hardening in Eq. (16), as

$$\dot{S}_r = h_{S_r}\dot{\lambda}, \quad h_{S_r} = \frac{-S_r^{sat}\min\left(\hat{\mathbf{P}}:\hat{\mathbf{N}},0\right) - S_r}{\Delta\varepsilon_r}, \quad S_r^{sat} = q_r R \tag{17}$$

In analogy with Eq. (16), the constant q_r relates the maximal strength contribution due to the reverse strain-path change to the isotropic hardening, $\Delta\varepsilon_r$ controls the strain scale for S_r to saturate towards the attractor $-S_r^{sat}\min\left(\hat{\mathbf{P}}:\hat{\mathbf{N}},0\right)$. The initial value of S_r is zero. Assume that $\hat{\mathbf{P}}$ is close to $\hat{\mathbf{N}}$ before the reversal of the strain-path takes place. Since $\hat{\mathbf{P}}:\hat{\mathbf{N}} = \|\hat{\mathbf{P}}\|\cos\phi$, then $\min\left(\hat{\mathbf{P}}:\hat{\mathbf{N}},0\right) = 0$. Note that the latter applies for any strain-path change for which $\phi \le 90°$. On the other hand, any strain-path change with $\phi > 90°$ has a reverse element. Then $\min\left(\hat{\mathbf{P}}:\hat{\mathbf{N}},0\right) < 0$, making the attractor in Eq. (17) positive. The contribution from S_r vanishes when the material adapts to the new deformation mode, i.e. as $\hat{\mathbf{P}}$ returns towards the actual strain path $\hat{\mathbf{N}}$.

3.5. Transient hardening due to the strain-path change

As reported in several papers (Li and Bate, 1991; Wilson et al., 1990; Zandrahimi et al., 1989) and as observed here for the aluminum AA1050, strain-path changes can, beside the transient effects, produce also persistent changes. If not only the flow stress but also the hardening rate is transiently changed due to the change in the strain path, this will cause a permanent effect on the flow stress. By using the ingredients of the model described above, i.e. isotropic hardening, kinematic hardening and extra contribution to isotropic hardening due to the orthogonal and reverse strain-path changes, it is implicitly assumed that stress-strain curves will eventually catch up with the monotonic reference tensile curve. In order to model the materials exhibiting permanent softening, the original model is extended by adding two additional contributions to the work hardening rate. This will cause the stress-strain curves, after a strain-path change, to deviate from the monotonic curve. The common interpretation is that the pre-formed anisotropic substructure causes not only the extra strength contribution after a strain-path change (S_o and S_r terms), but also directly influences the subsequent work hardening.

It is suggested that the orthogonal element of a strain-path change will cause reduction of the work hardening given as

$$h_o^{tr} = -k_o \left\|\hat{\mathbf{P}}\right\| \sin\phi \tag{18}$$

while the reverse element lowers the hardening rate as

$$h_r^{tr} = k_r \min\left(\hat{\mathbf{P}} : \hat{\mathbf{N}}, 0\right) \tag{19}$$

After the effect of the strain-path change vanishes and $\hat{\mathbf{P}}$ rotates towards actual strain path $\hat{\mathbf{N}}$, the contributions in Eqns. (18) and (19) fade out and the hardening rate returns back to that of monotonic straining. However, some strain is required to re-establish the hardening rate. The total isotropic hardening rate h_R can then be expressed as

$$h_R \equiv \frac{dR}{d\bar{\varepsilon}} = \sum_{i=1}^{2} h_{R_i} + h_o^{tr} + h_r^{tr} \tag{20}$$

Note that for materials not exhibiting permanent softening during orthogonal or reverse strain-path changes, contributions from h_o^{tr} and h_r^{tr} would be zero.

4. Parameter identification

For the calibration of the model a stand-alone implementation for calculations along single strain paths was made, allowing mixed prescription of components of the velocity gradient and stress components. Hence, all the strain paths of the tensile tests, including *r*-value variations could be predicted. To minimize the influence of aging, all test results used in the calibration of the model were obtained from tests with about one hour delay between the first and the second strain paths.

The model in its present form has all together 16 parameters (see Table 1). However, only 7 of them control the transient effects caused by substructural changes of the microstructure. This number further reduces down to 5 for materials not exhibiting permanent softening. The extended Voce rule involves 5 fitting parameters, whereas the extended Armstrong-Frederick rule has 4 model parameters.

Table 1: Model parameters

Isotropic hardening					Kinematic hardening			
R_0	R_1^{sat}	$\Delta\varepsilon_{R_1}$	R_2^{sat}	$\Delta\varepsilon_{R_2}$	X_1^{sat}	$\Delta\varepsilon_{X_1}$	X_2^{sat}	$\Delta\varepsilon_{X_2}$
[MPa]	[MPa]	[—]	[MPa]	[—]	[MPa]	[—]	[MPa]	[—]
14	76	0.34	28.4	0.025	3	0.067	3	0.003
Transient effects								
	$\Delta\varepsilon_P$	$\Delta\varepsilon_o$	$\Delta\varepsilon_r$	q_o	q_r	k_o	k_r	
	[—]	[—]	[—]	[—]	[—]	[MPa]	[MPa]	
	0.05	0.0004	0.01	0.16	0.2	115	1000	

The model parameters were identified from the monotonic tensile test, the Bauschinger tests and the orthogonal strain-path change tests. In the first step, the monotonic tensile test was used to fit the parameters R_0, R_1^{sat}, $\Delta\varepsilon_{R_1}$, R_2^{sat} and $\Delta\varepsilon_{R_2}$ of the extended Voce rule by the least squares method. In the second step, the stress-strain curves from the Bauschinger tests and the *r*-values from the orthogonal strain-path change tests were used to approximately adjust the parameters of the extended Armstrong-Frederick rule, namely X_1^{sat}, $\Delta\varepsilon_{X_1}$, X_2^{sat} and $\Delta\varepsilon_{X_2}$, without fitting the transient reverse hardening causing the stress plateau and the permanent softening, i.e. $S_r = 0$. In the third step, the parameters of the isotropic hardening rule had to be refitted for each set of the kinematic hardening parameters in order to get the monotonic curve correctly described. To this end, the least squares method was applied by minimizing the residual function

$$\mathbb{R} = \sum_k \left(R_0 + \sum_{i=1}^{2} R_i^{sat} \left(1 - \exp\left(-\frac{\varepsilon_k}{\Delta\varepsilon_{R_i}} \right) \right) + \sum_{i=1}^{2} X_i^{sat} \left(1 - \exp\left(-\frac{\varepsilon_k}{\Delta\varepsilon_{X_i}} \right) \right) - \sigma\left(\varepsilon_k\right) \right)^2 \tag{21}$$

where $\sigma_k \equiv \sigma\left(\varepsilon_k\right)$ is the experimentally obtained true stress at a true strain ε_k in the monotonic tensile test, and k runs over the measured points. In the fourth step, the transient hardening obtained from the Bauschinger tests and the orthogonal strain-path change tests was fitted. First, the parameter $\Delta\varepsilon_P$ controlling the rate of the substructure rebuilding, modeled by the evolution of the $\hat{\mathbf{P}}$ tensor, was assumed. Subsequently, the parameters $\Delta\varepsilon_r$, q_r and $\Delta\varepsilon_o$, q_o were found to get a best possible fit of both the transient reverse and orthogonal hardening, respectively. This was repeated for other values of parameter $\Delta\varepsilon_P$ until the best fit was obtained. The parameters controlling permanent softening k_o and k_r were adjusted simultaneously. Steps two to four were repeated until a satisfactory calibration was obtained. The resulting model parameters used are listed in Table 1.

The modeled stress-strain response after orthogonal and reverse strain-path changes are compared with the experimental data in Fig. 7. As can be seen, the proposed model can capture well both the overshoot of the flow stress after orthogonal strain-path change (Fig. 7a) and the stress plateau due to the strain-path reversal (Fig. 7b). The permanent softening effect is accounted for and governed by the Eqns. (18) and (19). For materials that do not exhibit any permanent softening, the variables k_o and k_r controlling the change of the hardening rate due to the strain-path change should be set to zero.

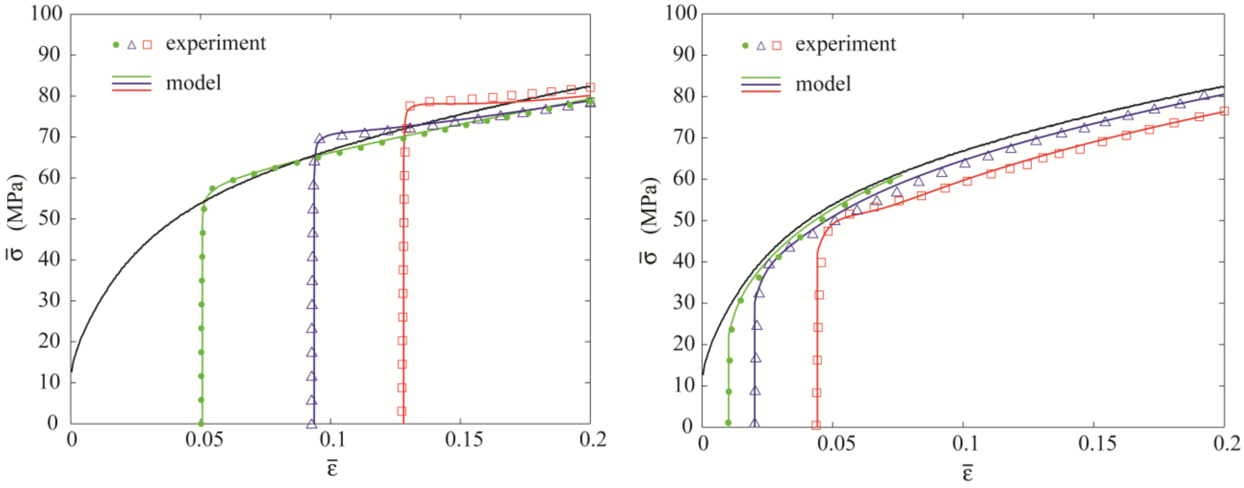

(a)

(b)

Fig. 7: (a) Comparison of the modeled and experimental effective stress-strain curves for (a) orthogonal strain-path changes introduced by the sequence rolling – uniaxial tension in transverse direction, after 5%, 9.3% and 12.8% of effective prestrain, and (b) reverse strain-path change introduced by the sequence compression – tension, with 1%, 2% and 4.4% prestrain, together with the monotonic stress-strain curve.

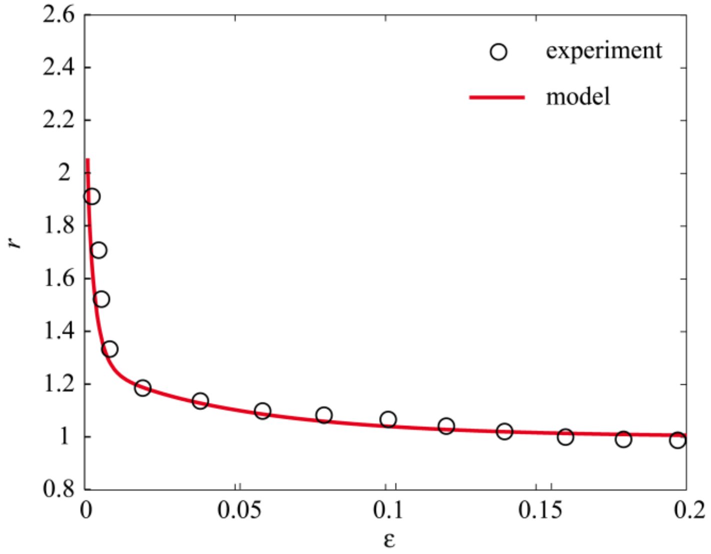

Fig. 8: Comparison of the modeled and measured *r*-values against true strain ε during the tensile tests after orthogonal strain-path changes with a prestrain of 5% by rolling.

The modeled transient change of the *r*-value during the tensile test after an orthogonal strain-path change with prestrain of 5% is shown in Fig. 8. The agreement with the experimental data is good. From the modeling point of view, the *r*-value reaches an increased value after the orthogonal strain-path change due to the distortion or shift of the yield locus caused by the first strain path. In the presented model, this is assumed to be caused by a combined effect of yield locus expansion and shift governed by the isotropic and kinematic hardening rules. Since two transients with different scales were observed experimentally, the extended Armstrong-Frederick rule defined by Eq. (13) was employed to model the kinematic hardening. It should also be noted, looking at the Bauschinger tests in Fig. 7b, that the strain scale for the micro-Bauschinger effect, i.e. the very high hardening rate between the yielding and the hardening stagnation, is very similar to that of the initial rapid change of the *r*-value after the orthogonal strain-path change. It may thus be anticipated that there is a common mechanism controlling the reorganization of the pre-built dislocation substructures at the very moments after instant strain-path changes. It seems that after any kind of instant strain-path change, orthogonal or reverse, the pre-formed dislocation substructures, e.g. pile-ups, are very unstable and will disappear within a very short strain. This process takes most probably place within the cell or subgrain interiors resulting in a very small mean-free path for moving dislocations (Hu et al., 1992). In the model, this is reflected by employing the extended Armstrong-Frederick kinematic rule containing two transients: a short one causing a rapid shift of the yield locus at very small strain, and a long, classical one, modeling the macro-Bauschinger effect itself, lasting during a much longer strain scale. The second strain path is thus always initiated by a rapid shift of the yield locus. In cases of orthogonal strain-path changes, this enables to model the fast transient change of the *r*-value, and superposed by the contribution from the extra strength S_o, the stress overshoot followed by softening can be captured. For the strain-path reversal, the micro-Bauschinger effect, as well as the characteristic plateau, can be modeled qualitatively by superposing the contribution from the extra strength S_r.

5. Finite element analysis

The continuum plasticity model was implemented as a user-defined material subroutine into the finite element software LS-DYNA, using the semi-implicit integration algorithm, as described in some detail in Appendix B. The explicit solver of LS-DYNA was used in the simulations.

The flat tensile specimen used in the tensile tests subsequent to rolling was meshed by quadratic 8 node solid elements with nodal rotations, i.e. 6 DOF per node, using selectively reduced integration. Four elements were used through the specimen thickness, 20 along the width and 50 along the gauge length. It was checked against an analytical solution that this discretization ensured a converged result. Mass scaling was used in the simulations, and it was checked carefully that the solution remained quasi-static.

In order to simulate the uniaxial tension being the second strain path subsequent to the rolling, all internal variables were conveniently initialized by values obtained by the stand-alone code, rather than first running an FEM simulation of the first strain path.

The force vs. engineering strain curves from the subsequent tension tests are plotted in Fig. 9 for the cases with prestrains of 9.3% and 12.8%. Good agreement is found between the experiments and the simulations. In particular, the premature necking in the test with the largest prestrain is captured accurately, while for the lower prestrain only incipient necking is observed as in the experiments. The FEM model could be run on an ordinary 2.7MHz PC in less than 20 minutes.

The predicted strain field in the test with 9.3% prestrain is shown in Fig. 10. The strain localization observed from the DIC analysis at a tensile strain of ~2%, see Fig. 4A, corresponds to the simulation of the strain field at the same engineering strain in Fig. 10A. The strain localization in the experiment is in the form of two crossed bands, but not crossing each other in the centre of the specimen as in the simulation. However, at least qualitatively, the simulated and experimental results are similar.

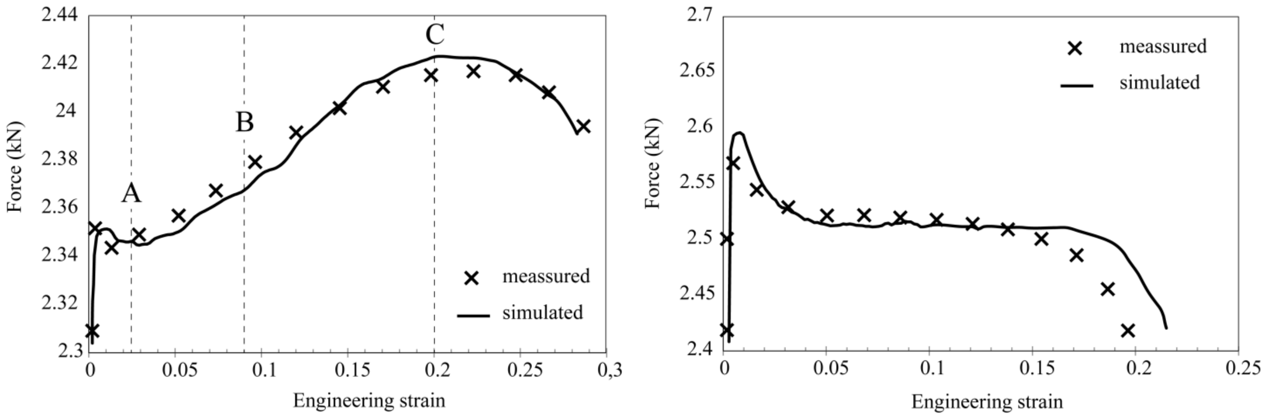

(a) (b)

Fig. 9: Comparison of the measured and simulated force vs. engineering strain during uniaxial tension for samples with effective prestrain of (a) 9.3% and (b) 12.8% due to the rolling.

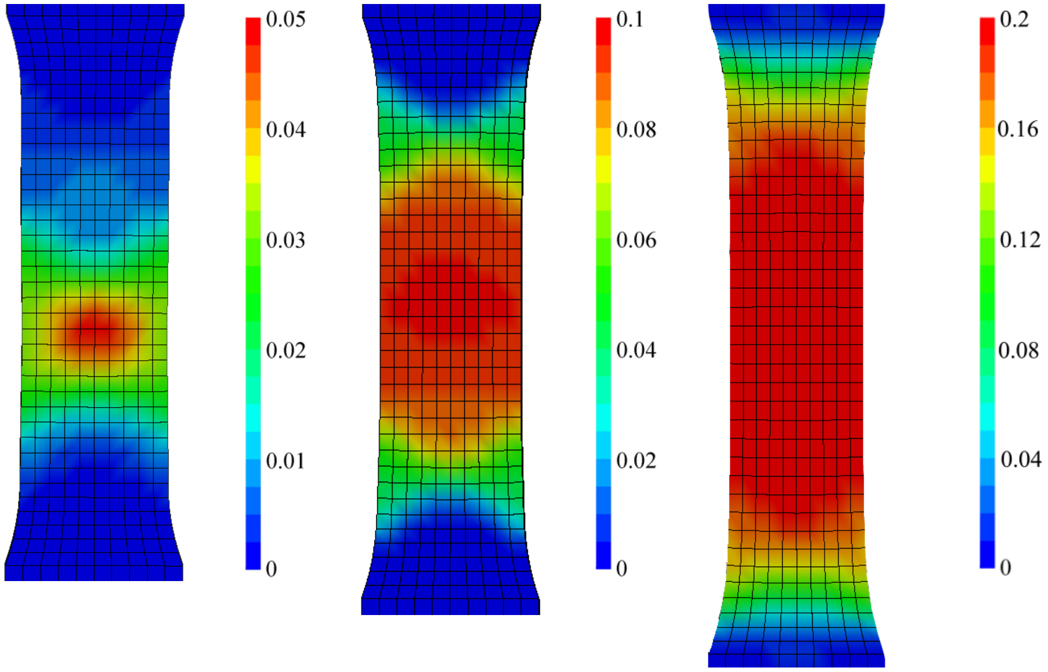

A B C

Fig. 10: The effective von Mises strain is shown for the finite element simulation of the uniaxial tension at engineering strains of 2.4% (A), 9% (B) and 20% (C) after prestrain to 9.3% in rolling.

6. Discussion

It is interesting to plot the tests in a Kocks-Mecking plot to see the work hardening characteristics. In Fig. 11, the plots are shown for 7 tests for the case of prestrains between 8.7% and 9.6% (Fig. 11a) and for 6 tests with prestrains between 11.1% and 12.8% (Fig. 11b) and the corresponding model predictions. In these diagrams, the normalized work-hardening rate $\bar{\theta}$ is plotted against the effective strain $\bar{\varepsilon}$, where

$$\bar{\theta} \equiv \frac{d\bar{\sigma}}{d\bar{\varepsilon}} \frac{1}{\bar{\sigma}} \tag{22}$$

Diffuse necking is expected to occur as $\bar{\theta}$ falls below unity, which is equivalent to the Considère criterion. From this point on, the experimental stretching becomes unstable and even though the conversion formulas are applied and the curves are plotted, one should keep in mind that the experimental curves are not strictly valid when $\bar{\theta}$ <1, then only the model results are valid. In the tensile tests a necking region spreads out similar as a Lüders band making the test non-uniform so that true stress and strain cannot be precisely predicted. This takes place very soon after yielding for two of the tests with prestrains 9.1% and 9.2%, shown as the red curves in Fig. 11a. However, the interval of strains for which $\bar{\theta} < 1$ is in this case very narrow (Fig. 11a) and the diffuse necking did not proceed beyond this early stage, i.e. after a small further elongation the work hardening is restored and the test continues by stable uniform straining (see also Zandrahimi et al. (1989)). On the other hand, for all the tests with prestrains larger than 11.1%, the decrease in the hardening rate after yielding did not enable restoration of a stable straining, which is indicated by the quantity $\bar{\theta}$ staying below unity. It can be seen from the model results that the work hardening catches up with the monotonic curve as the transient fades out. However, the stress at this point is lower, so that the stress-strain curve remains shifted a certain strain increment as compared to the monotonic one. Note that since the tensile tests are limited by the necking strain this model behavior cannot be validated. It might be that the experimental curves would converge at larger strains.

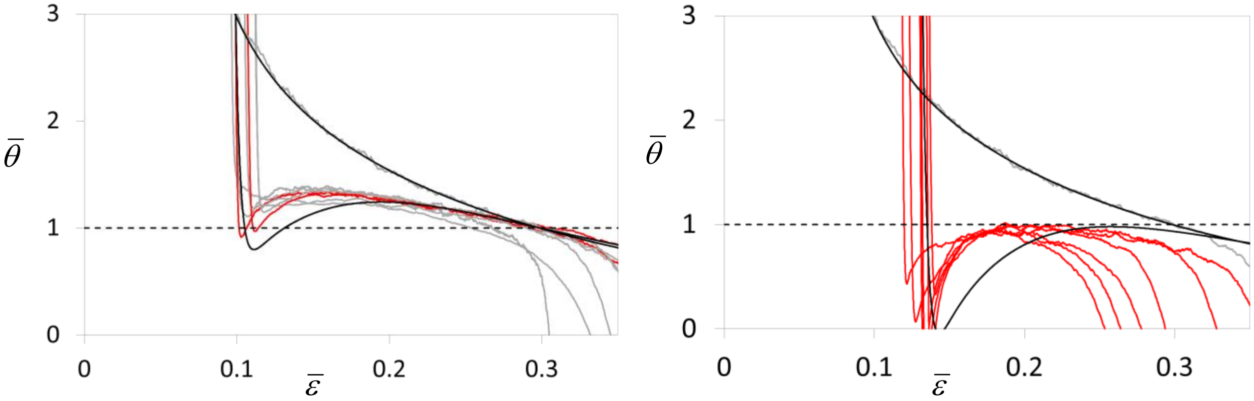

(a) (b)

Fig. 11: Plots of normalized work-hardening rate vs. effective strain for the monotonic curve and for prestrains (a) 9.3% and (b) 12.8%. Experimental curves are grey or red for tests for which the Considère criterion was reached at a very early stage after yielding. Black lines represent model predictions.

It can be seen from both the DIC and simulation results that the localized strains become distributed throughout the whole parallel section of the specimen, and due to sufficient subsequent increase of the hardening, quasi-uniform deformation was re-established at a strain of 0.09, cf. Fig. 4B and Fig. 10B. This type of behavior can only be captured when the transient behavior after a strain-path change is accounted for in the plasticity model.

In interstitial free steels, where the softening following an orthogonal strain path change is more pronounced, irreversible necking instability makes direct measurement of the material response during the transient challenging. The weaker effect in aluminum enables experiments without instability and reliable measurements at low pre-strains or subsequent to the re-establishment of the uniform deformation mode. True stress and strain, but also the *r*-value variation, can then be calculated from the test and allows probing the transient response of the metal. From Fig. 5, two distinct *r*-value transients with different strain scales can be seen. The *r*-value first changes rapidly from an average value of about 2.3 down to about 1.2 within a true tensile strain of 2-3%. After that, the change is much slower. The *r*-values reach the value of the monotonic straining equal to unity before the final necking occurs. Similar transient behavior of the *r*-value was observed for steel by Hutchinson and Davis (1983), but their measurements are less precise, since the they were made in the post-necking region.

For the two smallest prestrains the curves tend towards the monotonic curve as the transient fades away. However, for the largest prestrain a smaller stress level is reached within the largest strain before necking occurs. The aluminum AA1050 exhibits permanent softening, as observed by others as well (Li and Bate, 1991; Wilson et al., 1990; Zandrahimi et al., 1989). Quoting Li and Bate (1991): “The strain hardening rate following a strain-path change is markedly less than that for monotonic straining, at a given flow stress, over large deformation intervals.” Similarly as concluded by Wilson et al. (1990), the permanent softening at the total strain of 0.25 is about 5% of the monotonic flow stress.

The delayed pointer is a second-order tensor representing a memory of earlier strain paths. Both its magnitude and direction are changing as it is somehow trying to follow the current strain direction. If a strain-path is reversed, the delayed pointer will make the shortest way through the origin by first decreasing its magnitude to zero, and then increase it again, but now pointing in the opposite direction. On the other hand, if the path change is into an orthogonal direction the delayed pointer will partly rotate and partly change its magnitude during the transient. The magnitude and direction of the delayed pointer are thus assumed to represent the changing microstructure during non-proportional loading and its influence on the flow stress. The source of the microstructural effects can be for example build-up of aligned dislocation structures or latent hardening phenomena, but the proposed model is phenomenological and does not model these aspects in detail.

In the proposed model and other models of the same family as the Teodosiu-Hu model, the yield surface expands or shrinks in a shape invariant way. However, this is a simplification as the shape of the yield surface in general is changing. Experimental precise measurements at strains near the point of instant path change, Khan et al. (2010a, b), show that the yield surface in the early transient is heavily distorted. At larger strain increments away from the point of path change, the experimental work would be very challenging, because then a new experiment is required for each point on the locus and it becomes a challenge to filter out the scatter. Such experiments would contribute to an improved understanding of the transients but are beyond the scope of this work. The model proposed here provides a simplified approximation where the yield surface is not distorted.

Subsequent to an orthogonal strain path change the yield surface is rapidly expanded in the proposed model, thereby contributing with the correct amount of stress increase in the new orthogonal direction. Alternatively the shape of the yield surface can be distorted during the prestrain. This will correspond to the crystal plasticity model by Peeters et al. (2000) and Holmedal et al. (2008). In principle this can be obtained by a yield surface like the one proposed by Barlat et al. (2011). Whether the yield surface should be pre-distorted rather than rapidly expanded or shrunk subsequent to the strain-path change, can be sorted out by double strain-path change experiments like those recently reported by Vincze et al. (2013) and Barlat et al. (2014). This behavior might be material dependent. Probably some combination of the HAH and the Teodosiu-Hu type of approaches can provide an even better description of the strain-path change responses. Anyhow, the model proposed here represents a reasonable compromise regarding model complexity and prediction power in many applications.

7. Conclusions

Commercially pure, as-cast and homogenized aluminum AA1050 was prestrained either by rolling or by uniaxial compression and strain-path change tests were performed to study cross-hardening and Bauschinger transients of the flow stress. In addition, a transient variation of the *r*-value and a permanent reduction of the hardening subsequent to the strain-path changes were observed.

A recent continuum plasticity model, proposed originally by Holmedal et al. (2010), was modified to account for the experimental observations: the effects of the orthogonal and reverse strain-path changes, the permanent reduction of hardening, and the transient variation of the *r*-value. The constitutive model was implemented as a user-defined material subroutine in the finite element code LS-DYNA. The implementation has high computational efficiency as the anisotropy is represented by second-order tensors. The model was capable of reproducing the overshoot of the flow stress, the transient variation of the *r*-value and the permanent reduction of the hardening due to cross hardening for various prestrains, as well as the Bauschinger effect and the stress plateau typically occurring after strain-path reversals in commercially pure aluminium.

The strain localization took place after orthogonal strain-path changes for prestrains larger than about 9% for the given material. Using the DIC technique to measure the displacement field, it was observed in one case that diffuse necking was interrupted and uniform deformation was re-established. Finite element simulations using the proposed plasticity model provided a strain distribution in the sample in good agreement with the DIC observations and correctly described the diffuse necking process after the strain-path change. Thus the proposed model may be a good candidate among the continuum plasticity models to be applied in large-scale finite element analyses of forming processes.

Acknowledgment

Egil Fagerhaug is gratefully acknowledged for providing his own software for the DIC analysis.

Appendix A

The isotropic, high-exponent Hersey yield function (Hershey, 1954; Hosford, 1972) is defined as

$$\varphi(\boldsymbol{\sigma}') = \left(\frac{1}{2}\left(\left|\sigma_1' - \sigma_2'\right|^m + \left|\sigma_2' - \sigma_3'\right|^m + \left|\sigma_3' - \sigma_1'\right|^m \right) \right)^{1/m} \tag{23}$$

where $\boldsymbol{\sigma}'$ is the deviatoric Cauchy stress tensor and $\sigma_1', \sigma_2', \sigma_3'$ are the principal deviatoric stresses. In the case of plane strain compression, the deviatoric Cauchy stress $\boldsymbol{\sigma}'$ and the plastic strain rate tensor $\mathbf{D}^p$ can be expressed as

$$\boldsymbol{\sigma}' = \sigma_1' \begin{bmatrix} 1 & 0 & 0 \\ 0 & 0 & 0 \\ 0 & 0 & -1 \end{bmatrix}, \quad \mathbf{D}^p = D_1^p \begin{bmatrix} 1 & 0 & 0 \\ 0 & 0 & 0 \\ 0 & 0 & -1 \end{bmatrix} \tag{24}$$

where $D_1^p > 0$ is the major principal plastic strain rate. Combining Eqns. (23) and (24) gives

$$\varphi(\boldsymbol{\sigma}') = \sigma_1'\left(1+2^{m-1}\right)^{1/m} \tag{25}$$

By applying the yield condition

$$\bar{\sigma} \equiv \varphi(\boldsymbol{\sigma}') = \sigma_Y \tag{26}$$

where $\bar{\sigma}$ is the effective stress and σ_Y is the yield stress, the effective plastic strain rate $\dot{\bar{\varepsilon}}$ can be obtained from the plastic work rate as

$$\dot{W}^p = \boldsymbol{\sigma}' : \mathbf{D}^p = \bar{\sigma} \cdot \dot{\bar{\varepsilon}} \tag{27}$$

Substituting Eqns. (24)–(26) into Eq. (27) gives

$$\dot{\bar{\varepsilon}} = \left(2^{-m} + 2^{-1}\right)^{-1/m} D_1^p \tag{28}$$

Note that for $m = 2$ and $m = 4$, Eq. (28) gives the classical von Mises effective plastic strain rate $\dot{\bar{\varepsilon}}_{VM} = 2/\sqrt{3}\, D_1^p$. The functional dependence of $\dot{\bar{\varepsilon}} / D_1^p$ on m is plotted in Fig. 12. The Tresca yield function corresponding to the cases $m = 0$ and $m \to \infty$ leads to $\dot{\bar{\varepsilon}} / D_1^p = 1$ for plane strain compression. It is interesting to note that the maximum value of $\dot{\bar{\varepsilon}} / D_1^p$ corresponds to $m \approx 2.767$ for which the Hershey yield surface surrounds the greatest volume in stress space for a given value of the yield stress σ_Y.

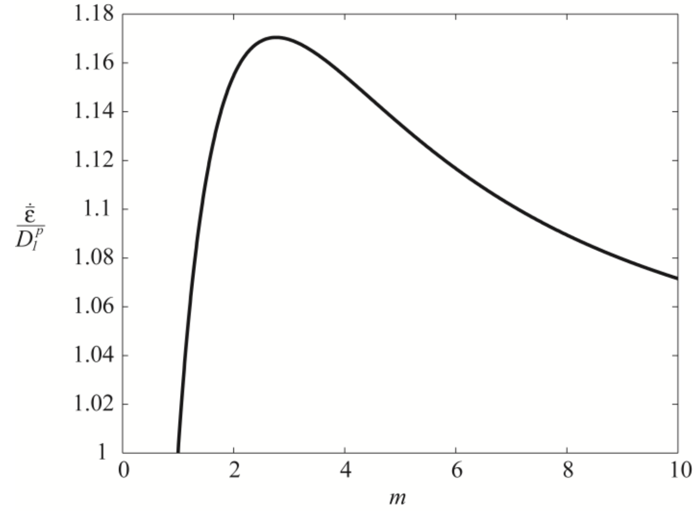

Fig. 12: Functional dependence of the ratio $\dot{\bar{\varepsilon}} / D_1^p$ on the exponent m in the high-exponent Hershey yield surface.

To derive the Schmitt angle, let us assume that the first strain path is by plane strain compression given by the plastic strain rate tensor $\mathbf{D}_1^p$ as

$$\mathbf{D}_1^p = D_1^p \begin{bmatrix} 1 & 0 & 0 \\ 0 & 0 & 0 \\ 0 & 0 & -1 \end{bmatrix} = \frac{\dot{\varepsilon}\left(1+2^{m-1}\right)^{1/m}}{2} \begin{bmatrix} 1 & 0 & 0 \\ 0 & 0 & 0 \\ 0 & 0 & -1 \end{bmatrix} \tag{29}$$

where $\dot{\varepsilon}_{VM} = \sqrt{\tfrac{2}{3}\mathbf{D}^p : \mathbf{D}^p}$ is the Von Mises effective plastic strain rate. If this is followed by uniaxial tension at an angle α with respect to the rolling direction, the plastic strain rate tensor $\mathbf{D}_2^p$ can be, for a given r-value, expressed as (similar as Holmedal et al. (2008) for the case of *m*=2)

$$\mathbf{D}_2^p = \frac{\dot{\varepsilon}\left(1+2^{m-1}\right)^{1/m}}{4\sqrt{r^2+r+1}} \begin{bmatrix} 1+(1+2r)\cos 2\alpha & (1+2r)\sin 2\alpha & 0 \\ (1+2r)\sin 2\alpha & 1-(1+2r)\cos 2\alpha & 0 \\ 0 & 0 & -2 \end{bmatrix} \tag{30}$$

The Schmitt angle according to Eq. (1) for such a strain-path change, is equal to

$$\phi = \arccos\left(\frac{3+(1+2r)\cos 2\alpha}{4\sqrt{r^2+r+1}} \right) \tag{31}$$

By doing the sequence of rolling and uniaxial tension in the rolling plane, one can, in theory, cover a range of Schmitt angles $\phi \in [0°, 120°]$ (see Fig. 13). However, for an isotropic material having *r*-values very close to 1, the Schmitt angles are limited between 30° and 90°.

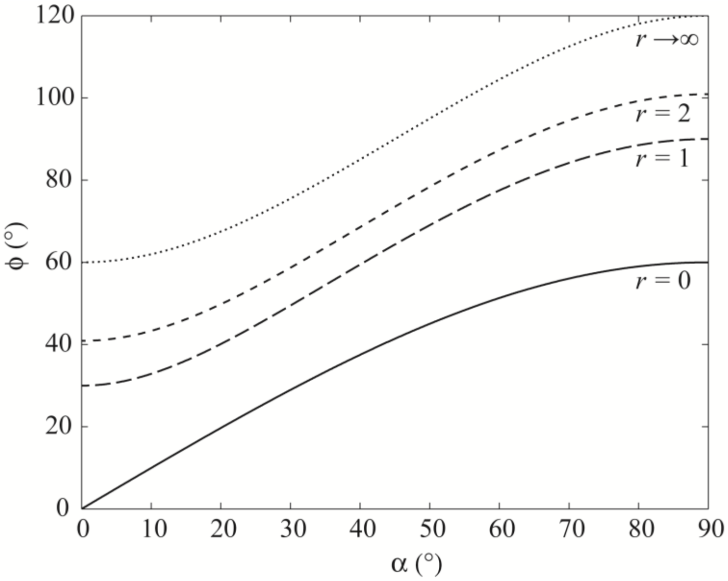

Fig. 13: Schmitt angle ϕ as a function of the angle α between uniaxial tension and rolling directions for *r*-values indicated in the figure.

Appendix B

A semi-implicit return map algorithm was developed for temporal integration of the rate constitutive equations (see e.g. Moran et al. (1990) and Belytschko et al. (2000)) and the proposed continuum plasticity model was implemented as a user-defined material subroutine in the finite element code LS-DYNA. The implementation is valid for explicit finite element methods.

The stress $\hat{\boldsymbol{\sigma}}_n$ and the internal variables $\hat{\mathbf{P}}_n$, $\hat{\mathbf{X}}_{i,n}$, R_n, $R_{i,n}$, $S_{o,n}$ and $S_{r,n}$ are assumed to be known at time step n. Let us denote the collection of internal variables as $\hat{\mathbf{q}}$ and their plastic moduli as $\hat{\mathbf{h}}$, so that $\dot{\hat{\mathbf{q}}} = \hat{\mathbf{h}}\dot{\lambda}$ represents the evolution equation for $\hat{\mathbf{q}}$. Given the strain increment $\Delta\hat{\boldsymbol{\varepsilon}}_{n+1} = \hat{\mathbf{D}}_{n+1}\Delta t_{n+1}$, where Δt_{n+1} is the time increment, the purpose of the constitutive integration algorithm is to compute the stress $\boldsymbol{\sigma}_{n+1}$ and the collection of internal variables $\hat{\mathbf{q}}_{n+1} = \left\{\hat{\mathbf{P}}_{n+1}, \hat{\mathbf{X}}_{i,n+1}, R_{n+1}, R_{i,n+1}, S_{o,n+1}, S_{r,n+1}\right\}$ at the time step $n+1$ while satisfying the yield condition

$$f_{n+1} \equiv f\left(\hat{\boldsymbol{\sigma}}_{n+1}, \hat{\mathbf{q}}_{n+1}\right) = \varphi\left(\hat{\boldsymbol{\sigma}}_{n+1} - \hat{\mathbf{X}}_{n+1}\right) - R_{n+1} - S_{o,n+1} - S_{r,n+1} = 0 \tag{32}$$

where $\hat{\mathbf{X}}_{n+1} = \sum_{i=1}^{2} \hat{\mathbf{X}}_{i,n+1}$. The algorithm starts with calculating the elastic predictor of the stress as

$$\hat{\boldsymbol{\sigma}}_{n+1}^{trial} = \hat{\boldsymbol{\sigma}}_n + \hat{\mathcal{C}} : \Delta\hat{\boldsymbol{\varepsilon}}_{n+1} \tag{33}$$

and checking whether the yield criterion for this trial stress is violated. If one obtains $f_{n+1}^{trial} = f\left(\hat{\boldsymbol{\sigma}}_{n+1}^{trial}, \hat{\mathbf{q}}_n\right) \leq 0$, then the trial step is purely elastic and the update at time step $n+1$ is done simply as

$$\boldsymbol{\sigma}_{n+1} = \hat{\boldsymbol{\sigma}}_{n+1}^{trial}, \quad \hat{\mathbf{q}}_{n+1} = \hat{\mathbf{q}}_n \tag{34}$$

On the other hand, if $f_{n+1}^{trial} = f\left(\hat{\boldsymbol{\sigma}}_{n+1}^{trial}, \hat{\mathbf{q}}_n\right) > 0$, then the step is elastic-plastic and a plastic corrector has to be determined in order to achieve consistency according to Eq. (32).

Before the return map algorithm is initiated, the normal to the yield surface $\hat{\mathbf{n}}_n \equiv \partial f\left(\hat{\boldsymbol{\sigma}}_n, \hat{\mathbf{q}}_n\right) / \partial\hat{\boldsymbol{\sigma}}_n$ and the plastic hardening moduli $\hat{\mathbf{h}}_n$ are computed using the state variables $\hat{\boldsymbol{\sigma}}_n$ and $\hat{\mathbf{q}}_n$ at time step n. The updated stress $\hat{\boldsymbol{\sigma}}_{n+1}$ and internal variables $\hat{\mathbf{q}}_{n+1}$ at time step $n+1$ are then given by

$$\hat{\boldsymbol{\sigma}}_{n+1} = \hat{\boldsymbol{\sigma}}_{n+1}^{trial} - \Delta\lambda_{n+1}\hat{\mathcal{C}} : \hat{\mathbf{n}}_n, \quad \hat{\mathbf{q}}_{n+1} = \hat{\mathbf{q}}_n + \Delta\lambda_{n+1}\hat{\mathbf{h}}_n \tag{35}$$

It is seen that this algorithm is implicit in the plastic parameter $\Delta\lambda_{n+1}$, while the plastic flow direction $\hat{\mathbf{n}}_n$ and the hardening moduli $\hat{\mathbf{h}}_n$, evaluated at the previous time step n, are kept constant during the iterations. This semi-implicit stress update scheme is an efficient and robust algorithm allowing simple implementation of complex constitutive models but the strain increments should not be too large. This makes the algorithms particularly suited for explicit finite element methods where time steps are usually very small, thus limiting the strain increments.

Combination of Eqns. (32) and (35) provides a nonlinear equation for $\Delta\lambda_{n+1}$ which is solved by employing the Newton procedure. The equation $f\left(\Delta\lambda_{n+1}\right) = 0$ is linearized in iteration (k) as

$$f\left(\Delta\lambda_{n+1}^{(k)}\right)+\frac{df_{n+1}^{(k)}}{d\Delta\lambda_{n+1}^{(k)}}\delta\lambda_{n+1}^{(k)}=0 \tag{36}$$

where we have used the notation $f_{n+1}^{(k)} \equiv f\left(\Delta\lambda_{n+1}^{(k)}\right)$, and from which increment $\delta\lambda_{n+1}^{(k)}$ is used to update the $\Delta\lambda_{n+1}$ in iteration $(k+1)$ as

$$\Delta\lambda_{n+1}^{(k+1)}=\Delta\lambda_{n+1}^{(k)}+\delta\lambda_{n+1}^{(k)} \tag{37}$$

where $\delta\lambda_{n+1}^{(k)}$ is estimated as

$$\delta\lambda_{n+1}^{(k)}=\frac{f_{n+1}^{(k)}}{\hat{\mathbf{n}}_n:\hat{\mathcal{C}}:\hat{\mathbf{n}}_n+\hat{\mathbf{n}}_n:\hat{\mathbf{h}}_{X,n}+h_{R,n}+h_{S_o,n}+h_{S_r,n}} \tag{38}$$

The iteration process continues until

$$\frac{f_{n+1}^{(k+1)}}{\bar{\sigma}_{n+1}^{(k+1)}}<\xi \tag{39}$$

where a typical value of the tolerance ξ is 10^{-6}; $\bar{\sigma}_{n+1}^{(k+1)}$ being the current value of the effective stress with respect to the back stress. At the end of the iteration process, the plastic parameter $\Delta\lambda_{n+1}$ is obtained, and the stress and the internal variables can be updated according to Eq. (35).

References

Armstrong, P.J., Frederick, C.O., 1966. A mathematical representation of the multiaxial Bauschinger effect. , GEGB Report RD/B/N731.

Baltov, A., Sawczuk, A., 1965. A rule of anisotropic hardening. Acta Mechanica 1, 81-92.

Barlat, F., 1987. Crystallographic texture, anisotropic yield surfaces and forming limits of sheet metals. Materials Science and Engineering 91, 55-72.

Barlat, F., Duarte, J.M.F., Gracio, J.J., Lopes, A.B., Rauch, E.F., 2003. Plastic flow for non-monotonic loading conditions of an aluminum alloy sheet sample. Int. J. Plast. 19, 1215-1244.

Barlat, F., Gracio, J.J., Lee, M.G., Rauch, E.F., Vincze, G., 2011. An alternative to kinematic hardening in classical plasticity. Int. J. Plast. 27, 1309-1327.

Barlat, F., Ha, J., Gracio, J.J., Lee, M.-G., Rauch, E.F., Vincze, G., 2013. Extension of homogeneous anisotropic hardening model to cross-loading with latent effects. Int. J. Plast. 46, 130-142.

Barlat, F., Vincze, G., Gracio, J.J., Lee, M.G., Rauch, E.F., Tomé, C.N., 2014. Enhancements of homogeneous anisotropic hardening model and application to mild and dual-phase steels. Int. J. Plast. 58, 201-218.

Barthel, C., Levkovitch, V., Svendsen, B., 2008. Modeling of sheet metal forming processes taking into account distortional hardening. Int. J. Mater. Form. 1, 105-108.

Bate, P.S., Brough, I., Morse, S., 2007. Static recovery and the orthogonal strain path change effect in IF steel, in: Prangnell, P.B., Bate, P.S. (Eds.), Fundamentals of Deformation and Annealing. Trans Tech Publications Ltd, Stafa-Zurich, pp. 141-148.

Bauschinger, J., 1881. Changes of the elastic limit and the modulus of elasticity on various metals. Civilingenieur 27, 289-348.

Belytschko, T., Liu, W.K., Moran, B., 2000. Nonlinear Finite Elements for Continua and Structures. Wiley.

Benallal, A., Berstad, T., Borvik, T., Hopperstad, O.S., Koutiri, I., de Codes, R.N., 2008. An experimental and numerical investigation of the behaviour of AA5083 aluminium alloy in presence of the Portevin-Le Chatelier effect. Int. J. Plast. 24, 1916-1945.

Boers, S.H.A., Schreurs, P.J.G., Geers, M.G.D., Levkovitch, V., Wang, J., Svendsen, B., 2010. Experimental characterization and model identification of directional hardening effects in metals for complex strain path changes. Int. J. Solids Struct. 47, 1361-1374.

Bouvier, S., Alves, J.L., Oliveira, M.C., Menezes, L.F., 2005. Modelling of anisotropic work-hardening behaviour of metallic materials subjected to strain-path changes. Comput. Mater. Sci. 32, 301-315.

Brown, D.W., Beyerlein, I.J., Sisneros, T.A., Clausen, B., Tomé, C.N., 2012. Role of twinning and slip during compressive deformation of beryllium as a function of strain rate. Int. J. Plast. 29, 120-135.

Brown, L.M., 1977. Orowan explanation of Bauschinger effect. Scripta Metallurgica 11, 127-131.

Brown, L.M., Stobbs, W.M., 1971. Work-hardening of copper-silica. 2. Role of plastic relaxation. Philosophical Magazine 23, 1201-&.

Butuc, M.A., Barlat, F., Gracio, J.J., da Rocha, A.B., 2010. A new model for FLD prediction based on advanced constitutive equations. Int. J. Mater. Form. 3, 191-204.

Butuc, M.C., Barlat, F., Gracio, J.J., 2011. Study on plastic flow localization prediction using a physically-based hardening model. Comput. Mater. Sci. 50, 2688–2697.
Carvalho-Resende, T., Balan, T., Bouvier, S., Abed-Meraim, F., Sablin, S.S., 2013. Numerical investigation and experimental validation of a plasticity model for sheet steel forming. Model. Simul. Mater. Sci. Eng. 21.
Choi, Y., Han, C.S., Lee, J.K., Wagoner, R.H., 2006. Modeling multi-axial deformation of planar anisotropic elasto-plastic materials, part 1: Theory. Int. J. Plast. 22, 1745-1764.
Clausmeyer, T., Noman, M., Svendsen, B., 2009. Comparison of two models for anisotropic hardening evolution in metals during complex loading. Int. J. Mater. Form. 2, 395-398.
da Rocha, A.B., Santos, A.D., Teixeira, P., Butuc, M.C., 2009. Analysis of plastic flow localization under strain paths changes and its coupling with finite element simulation in sheet metal forming. J. Mater. Process. Technol. 209, 5097-5109.
De Codes, R.N., Hopperstad, O.S., Engler, O., Lademo, O.G., Embury, J.D., Benallal, A., 2011. Spatial and Temporal Characteristics of Propagating Deformation Bands in AA5182 Alloy at Room Temperature. Metall. Mater. Trans. A-Phys. Metall. Mater. Sci. 42A, 3358-3369.
Eardley, E.S., Soulet, A., Court, S.A., Humphreys, F.J., Bate, P.S., 2003. Microstructure and plastic anisotropy in rolled Al-Mg alloys, in: Chandra, T., Torralba, J.M., Sakai, T. (Eds.), Thermec'2003, Pts 1-5. Trans Tech Publications Ltd, Zurich-Uetikon, pp. 363-368.
Esche, S.K., Ahmetoglu, M.A., Kinzel, G.L., Altan, T., 2000. Numerical and experimental investigation of redrawing of sheet metals. J. Mater. Process. Technol. 98, 17-24.
Fagerholt, E., 2012. Field Measurements in Mechanical Testing Using Close-Range Photogrammetry and Digital Image Analysis, Department of Structural Engineering. Norwegian University of Science and Technology, Trondheim.
Feigenbaum, H.P., Dafalias, Y.F., 2007. Directional distortional hardening in metal plasticity within thermodynamics. Int. J. Solids Struct. 44, 7526-7542.
Flores, P., Duchene, L., Bouffioux, C., Lelotte, T., Henrard, C., Pernin, N., Van Bael, A., He, S., Duflou, J., Habraken, A.M., 2007. Model identification and FE simulations: Effect of different yield loci and hardening laws in sheet forming. Int. J. Plast. 23, 420-449.
Francois, M., 2001. A plasticity model with yield surface distortion for non proportional loading. Int. J. Plast. 17, 703-717.
Franz, G., Abed-Meraim, F., Berveiller, M., 2013. Strain localization analysis for single crystals and polycrystals: Towards microstructure-ductility linkage. Int. J. Plast. 48, 1-33.
Garofalo, F., Low, J.R., 1955. The effect of prestraining in simple tension and biaxial tension on flow and fracture behaviour of a low carbon deep-drawing steel sheet. J. Mech. Phys. Solids 3, 275-294.
Ghosh, A.K., Backofen, W.A., 1973. Strain-hardening and instability in biaxially stretched sheets. Metallurgical Transactions 4, 1113-1123.
Ha, J., Lee, M.G., Barlat, F., 2013. Strain hardening response and modeling of EDDQ and DP780 steel sheet under non-linear strain path, Mech. Mater.
Haddadi, H., Bouvier, S., Banu, M., Maier, C., Teodosiu, C., 2006. Towards an accurate description of the anisotropic behaviour of sheet metals under large plastic deformations: Modelling, numerical analysis and identification. Int. J. Plast. 22, 2226-2271.
Haddag, B., Balan, T., Abed-Meraim, F., 2007. Investigation of advanced strain-path dependent material models for sheet metal forming simulations. Int. J. Plast. 23, 951-979.
Hershey, A.V., 1954. The plasticity of an isotropic aggregate of anisotropic face-centered cubic crystals. J. Appl. Mech.-Trans. ASME 21, 241-249.

Hiwatashi, S., Van Bael, A., Van Houtte, P., Teodosiu, C., 1997. Modelling of plastic anisotropy based on texture and dislocation structure. Comput. Mater. Sci. 9, 274-284.
Hoc, T., Rey, C., Raphanel, J.L., 2001. Experimental and numerical analysis of localization during sequential test for an IF-Ti steel. Acta Materialia 49, 1835-1846.
Holmedal, B., Hopperstad, O.S., Berstad, T., 2010. Modeling Transients Related to Strain-path Changes, in: Kumai, S., Umezawa, O., Takayama, Y., Tsuchida, T., Sato, T. (Eds.), 11th. International Conference of Aluminium Alloys. The Japan Institute of Light Metals, Yokohama, Japan.
Holmedal, B., Van Houtte, P., An, Y.G., 2008. A crystal plasticity model for strain-path changes in metals. Int. J. Plast. 24, 1360-1379.
Hosford, W.F., 1972. A Generalized Isotropic Yield Criterion. Journal of Applied Mechanics 39, 607-609.
Hosford, W.F., 2010. Mechanical behavior of materials. Cambridge University Press, Cambridge, United Kingdom.
Hu, Z.Q., Rauch, E.F., Teodosiu, C., 1992. Work-hardening behavior of mild-steel under stress reversal at large strains. Int. J. Plast. 8, 839-856.
Hutchinson, W.B., Arthey, R., Malmstrom, P., 1976. Anomalously low work-hardening in pre-strained metals. Scripta Metallurgica 10, 673-675.
Hutchinson, W.B., Davis, T., 1983. The effect of non-linear strain paths on the plastic properties of steels, in: Carlsson, J., Ohlson, N.G. (Eds.), Mechanical Behaviour of Materials. Pergamon Press, Stockholm, Sweden, pp. 1227-1233.
Ishikawa, H., 1997. Subsequent yield surface probed from its current center. Int. J. Plast. 13, 533-549.
Ishikawa, H., Sasaki, K., 1998. Deformation induced anisotropy and memorized back stress in constitutive model. Int. J. Plast. 14, 627-646.
Jensen, D.J., Hansen, N., 1990. Flow-stress anisotropy in aluminum. Acta Metall. Mater. 38, 1369-1380.
Khan, A.S., Kazmi, R., Pandey, A., Stoughton, T., 2009. Evolution of subsequent yield surfaces and elastic constants with finite plastic deformation. Part-I: A very low work hardening aluminum alloy (Al6061-T6511). Int. J. Plast. 25, 1611-1625.
Khan, A.S., Pandey, A., Stoughton, T., 2010a. Evolution of subsequent yield surfaces and elastic constants with finite plastic deformation. Part II: A very high work hardening aluminum alloy (annealed 1100 Al). Int. J. Plast. 26, 1421-1431.
Khan, A.S., Pandey, A., Stoughton, T., 2010b. Evolution of subsequent yield surfaces and elastic constants with finite plastic deformation. Part III: Yield surface in tension–tension stress space (Al 6061–T 6511 and annealed 1100 Al). Int. J. Plast. 26, 1432-1441.
Korbel, A., Martin, P., 1988. Microsctructural events of macroscopic strain localization in prestrained tensile specimens. Acta Metallurgica 36, 2575-2586.
Lamba, H.S., Sidebottom, O.M., 1978a. Cyclic plasticity for non-proportional paths. 1. Cyclic hardening, erasure of memory, and subsequent strain-hardening experiments. J. Eng. Mater. Technol.-Trans. ASME 100, 96-103.
Lamba, H.S., Sidebottom, O.M., 1978b. Cyclic plasticity for non-proportional paths. 2. Comparison with predicitons of three incremental plasticity models. J. Eng. Mater. Technol.-Trans. ASME 100, 104-111.
Laukonis, J.V., 1979. Anisotropic strain localization in tensile prestrained sheet steel. Journal of Metals 31, 35-35.

Laukonis, J.V., Ghosh, A.K., 1978. Effects of strain path changes on the formability of sheet metals. Metallurgical Transactions a-Physical Metallurgy and Materials Science 9, 1849-1856.

Lee, J.W., Lee, M.G., Barlat, F., 2012. Finite element modeling using homogeneous anisotropic hardening and application to spring-back prediction. Int. J. Plast. 29, 13-41.

Levkovitch, V., Svendsen, B., 2007a. Accurate hardening modeling as basis for the realistic simulation of sheet forming processes with complex strain-path changes, in: Cueto, E., Chinesta, F. (Eds.), 10th ESAFORM Conference on Material Forming, Pts A and B. Amer Inst Physics, Melville, pp. 358-363.

Levkovitch, V., Svendsen, B., 2007b. Accurate hardening modeling as basis for the realistic simulation of sheet forming processes with complex strain-path changes, in: CeasarDeSa, J.M.A., Santos, A.D. (Eds.), NUMIFORM '07: Materials Processing and Design: Modeling, Simulation and Applications, Pts I and II. Amer Inst Physics, Melville, pp. 1331-1336.

Li, F., Bate, P.S., 1991. Strain path change effects in cube textured aluminum sheet. Acta Metall. Mater. 39, 2639-2650.

Li, S.Y., Hoferlin, E., Van Bael, A., Van Houtte, P., Teodosiu, C., 2003. Finite element modeling of plastic anisotropy induced by texture and strain-path change. Int. J. Plast. 19, 647-674.

Li, Z.J., Winther, G., Hansen, N., 2004. Anisotropy of plastic deformation in rolled aluminum. Mater. Sci. Eng. A-Struct. Mater. Prop. Microstruct. Process. 387, 199-202.

Li, Z.J., Winther, G., Hansen, N., 2006. Anisotropy in rolled metals induced by dislocation structure. Acta Materialia 54, 401-410.

Lloyd, D.J., Sang, H., 1979. Influence of strain path on subsequent mechanical properties - orthogonal tensile paths. Metallurgical Transactions a-Physical Metallurgy and Materials Science 10, 1767-1772.

Manik, T., Holmedal, B., Hopperstad, O.S., 2012. Modeling of Transients as a Response to Changes in Strain–Path of Commercially Pure Aluminium, in: Weiland, H., Rollett, A.D., Cassada, W.A. (Eds.), 13th International Conference on Aluminum Alloys. Wiley, Pittsburgh, Pennsylvania, USA.

Moran, B., Ortiz, M., Shih, C.F., 1990. Formulation of implicit finite-element methods for multiplicative finite deformation plasticity. Int. J. Numer. Methods Eng. 29, 483-514.

Noman, M., Clausmeyer, T., Barthel, C., Svendsen, B., Huetink, J., van Riel, M., 2010. Experimental characterization and modeling of the hardening behavior of the sheet steel LH800. Mater. Sci. Eng. A-Struct. Mater. Prop. Microstruct. Process. 527, 2515-2526.

Oliveira, M.C., Alves, J.L., Chaparro, B.M., Menezes, L.F., 2007. Study on the influence of work-hardening modeling in springback prediction. Int. J. Plast. 23, 516-543.

Pandey, A., Khan, A.S., Kim, E.-Y., Choi, S.-H., Gnäupel-Herold, T., 2013. Experimental and numerical investigations of yield surface, texture, and deformation mechanisms in AA5754 over low to high temperatures and strain rates. Int. J. Plast. 41, 165-188.

Peeters, B., Kalidindi, S.R., Van Houtte, P., Aernoudt, E., 2000. A crystal plasticity based work-hardening/softening model for b.c.c. metals under changing strain paths. Acta Materialia 48, 2123-2133.

Peeters, B., Seefeldt, M., Teodosiu, C., Kalidindi, S.R., Van Houtte, P., Aernoudt, E., 2001. Work-hardening/softening behaviour of b.c.c. polycrystals during changing strain paths: I. An integrated model based on substructure and texture evolution, and its prediction of the stress–strain behaviour of an IF steel during two-stage strain paths. Acta Materialia 49, 1607-1619.

Pietryga, M.P., Vladimirov, I.N., Reese, S., 2012. A finite deformation model for evolving flow anisotropy with distortional hardening including experimental validation. Mech. Mater. 44, 163-173.

Proust, G., Kaschner, G.C., Beyerlein, I.J., Clausen, B., Brown, D.W., McCabe, R.J., Tome, C.N., 2010. Detwinning of High-Purity Zirconium: In-Situ Neutron Diffraction Experiments. Experimental Mechanics 50, 125-133.

Rastogi, P.K., 2000. Photomechanics. Springer, Berlin, Germany.

Rauch, E.F., Gracio, J.J., Barlat, F., Vincze, G., 2011. Modelling the plastic behaviour of metals under complex loading conditions. Model. Simul. Mater. Sci. Eng. 19.

Reis, A., Santos, A.D., Duarte, J.F., Rocha, A.B., Li, S.Y., Hoferlin, E., Van Bael, A., Van Houtte, P., Teodosiu, C., 2002. Finite-element simulation and experimental validation of a plasticity model of texture and strain-induced anisotropy, in: Vieira, T. (Ed.), Advanced Materials Forum I. Trans Tech Publications Ltd, Zurich-Uetikon, pp. 501-504.

Roters, F., Eisenlohr, P., Bieler, T.R., Raabe, D., 2010. Crystal Plasticity Finite Element Methods. Wiley-VCH Verlag, Singapore.

Roux, S., Rethore, J., Hild, F., 2008. Recent progress in digital image correlation: From measurement to mechanical identification. Journal of Physics: Conference Series 135.

Sakharova, N.A., Vieira, M.M., Fernandes, J.V., Vieira, M.F., 2008. Strain Path Change Effect on Deformation Behaviour of Materials with Low-to-Moderate Stacking Fault Energy, in: Marques, A.T., Silva, A.F., Baptista, A.P.M., Sa, C., Alves, F., Malheiros, L.F., Vieira, M. (Eds.), Advanced Materials Forum Iv. Trans Tech Publications Ltd, Stafa-Zurich, pp. 420-424.

Schmitt, J.H., Aernoudt, E., Baudelet, B., 1985. Yield loci for polycrystalline metals without texture. Materials Science and Engineering 75, 13-20.

Schmitt, J.H., Fernandes, J.V., Gracio, J.J., Vieria, M.F., 1991. Plastic behavior of copper sheets during sequential tension tests. Mater. Sci. Eng. A-Struct. Mater. Prop. Microstruct. Process. 147, 143-154.

Seipp, S., Wagner, M.F.X., Hockauf, K., Schneider, I., Meyer, L.W., Hockauf, M., 2012. Microstructure, crystallographic texture and mechanical properties of the magnesium alloy AZ31B after different routes of thermo-mechanical processing. Int. J. Plast. 35, 155-166.

Shi, B., Mosler, J., 2013. On the macroscopic description of yield surface evolution by means of distortional hardening models: Application to magnesium. Int. J. Plast. 44, 1-22.

Sisneros, T.A., Brown, D.W., Clausen, B., Donati, D.C., Kabra, S., Blumenthal, W.R., Vogel, S.C., 2010. Influence of strain rate on mechanical properties and deformation texture of hot-pressed and rolled beryllium. Materials Science and Engineering: A 527, 5181-5188.

Sivaraman, A., Chakkingal, U., 2008. Flow properties of commercial purity aluminum processed by equal channel angular pressing. Mater. Sci. Eng. A-Struct. Mater. Prop. Microstruct. Process. 487, 264-270.

Sun, L., Wagoner, R.H., 2013. Proportional and non-proportional hardening behavior of dual-phase steels. Int. J. Plast. 45, 174-187.

Sutton, M.A., McNeill, S.R., Helm, J.D., Chao, Y.J., 2000. Advances in two-dimensional and three-dimensional computer vision. Photo-Mechanics 77, 323-372.

Taylor, G.I., 1938. Plastic strain in metals. J Inst Metals 62, 307-324.

Teodosiu, C., Hu, Z.Q., 1995. Evolution of the intragranular microstructure at moderate and large strains - modelling and computational significance. A a Balkema, Rotterdam.

Thuillier, S., Manach, P.Y., Menezes, L.F., 2010. Occurence of strain path changes in a two-stage deep drawing process. J. Mater. Process. Technol. 210, 226-232.

Uenishi, A., Teodosiu, C., 2004. Constitutive modelling of the high strain rate behaviour of interstitial-free steel. Int. J. Plast. 20, 915-936.
Van Den Boogaard, A.H., Van Riel, M., 2009. Non-proportional deformation paths for sheet metal: experiments and models, Forming Technology Forum, ETH Zurich, Switzerland.
Vincze, G., Barlat, F., Rauch, E.F., Tome, C.N., Butuc, M.A., Gracio, J.J., 2013. Experiments and Modeling of Low Carbon Steel Sheet Subjected to Double Strain Path Changes. Metall. Mater. Trans. A-Phys. Metall. Mater. Sci. 44, 4475-4479.
Vincze, G., Rauch, E.F., Gracio, J.J., Barlat, F., Lopes, A.B., 2005. A comparison of the mechanical behaviour of an AA1050 and a low carbon steel deformed upon strain reversal. Acta Materialia 53, 1005-1013.
Voce, E., 1948. The Relationship between Stress and Strain for Homogeneous Deformation. Journal of the Institute of Metals 74, 537-562.
Wagoner, R.H., Laukonis, J.V., 1983. Plastic behavior of aluminum-killed steel following plane-strain deformation. Metallurgical Transactions a-Physical Metallurgy and Materials Science 14, 1487-1495.
Wang, J., Levkovitch, V., Reusch, F., Svendsen, B., Huetink, J., van Riel, M., 2008. On the modeling of hardening in metals during non-proportional loading. Int. J. Plast. 24, 1039-1070.
Wang, J., Levkovitch, V., Svendsen, B., 2006. Modeling and simulation of directional hardening in metals during non-proportional loading. J. Mater. Process. Technol. 177, 430-432.
Wilson, D.V., 1994. Influences of cell-walls and grain-boundaries on transient responses of an IF steel to changes in strain path. Acta Metall. Mater. 42, 1099-1111.
Wilson, D.V., Zandrahimi, M., Roberts, W.T., 1990. Effects of changes in strain path on work-hardening in CP aluminum and an Al-Cu-Mg alloy. Acta Metall. Mater. 38, 215-226.
Yapici, G.G., Beyerlein, I.J., Karaman, I., Tome, C.N., 2007. Tension-compression asymmetry in severely deformed pure copper. Acta Materialia 55, 4603-4613.
Yoshida, K., Kuroda, M., 2012. Comparison of bifurcation and imperfection analyses of localized necking in rate-independent polycrystalline sheets. Int. J. Solids Struct. 49, 2073-2084.
Zandrahimi, M., Platias, S., Price, D., Barrett, D., Bate, P.S., Roberts, W.T., Wilson, D.V., 1989. Effects of changes in strain path on work-hardening in cubic metals. Metallurgical Transactions a-Physical Metallurgy and Materials Science 20, 2471-2482.